

AD-A132 297

TURBULENT WALL PRESSURE SIMULATION(U) OLD DOMINION UNIV
NORFOLK VA DEPT OF MECHANICAL ENGINEERING AND MECHANICS
M R KHORRAMI JUL 83 N00014-82-K-0639

1/1

UNCLASSIFIED

F/G 20/4

NL

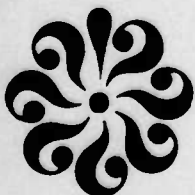




MICROCOPY RESOLUTION TEST CHART
NATIONAL BUREAU OF STANDARDS-1963-A

AD A 1 3 2 2 9 7

DTIC FILE COPY



OLD DOMINION UNIVERSITY RESEARCH FOUNDATION

12

DEPARTMENT OF MECHANICAL ENGINEERING AND MECHANICS
SCHOOL OF ENGINEERING
OLD DOMINION UNIVERSITY
NORFOLK, VIRGINIA

TURBULENT WALL PRESSURE SIMULATION

By

Robert L. Ash, Principal Investigator

and

Mehdi R. Khorrami

Final Report

For the period ending June 30, 1983

Prepared for the
Department of the Navy
Office of Naval Research
800 N. Quincy St.
Arlington, Virginia 22217

DTIC
ELECTE
S SEP 8 1983 D
B

Under
Research Grant N00014-82-K-0639
Task No. NR 657-694
Dr. M. M. Reischman, ONR Scientific Officer

Approved for public release; distribution
unlimited. Reproduction in whole or in part is
permitted for any purpose of the United States
Government.

July 1983

83 09 01 001

DEPARTMENT OF MECHANICAL ENGINEERING AND MECHANICS
SCHOOL OF ENGINEERING
OLD DOMINION UNIVERSITY
NORFOLK, VIRGINIA

TURBULENT WALL PRESSURE SIMULATION

By

Robert L. Ash, Principal Investigator

and

Mehdi R. Khorrami

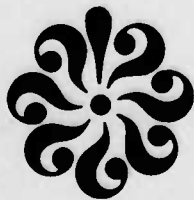
Final Report

For the period ending June 30, 1983

Prepared for the
Department of the Navy
Office of Naval Research
800 N. Quincy St.
Arlington, Virginia 22217

Under
Research Grant N00014-82-K-0639
Task No. NR 657-694
Dr. M. M. Reischman, ONR Scientific Officer

Submitted by the
Old Dominion University Research Foundation
P.O. Box 6369
Norfolk, Virginia 23508



July 1983

Unclassified

SECURITY CLASSIFICATION OF THIS PAGE (When Data Entered)

REPORT DOCUMENTATION PAGE		READ INSTRUCTIONS BEFORE COMPLETING FORM
1. REPORT NUMBER 1	2. GOVT ACCESSION NO.	3. RECIPIENT'S CATALOG NUMBER
4. TITLE (and Subtitle) Turbulent Wall Pressure Simulation		5. TYPE OF REPORT & PERIOD COVERED FINAL July 1982 - June 1983
		6. PERFORMING ORG. REPORT NUMBER
7. AUTHOR(s) Robert L. Ash, Principal Investigator Mehdi R. Khorrami		8. CONTRACT OR GRANT NUMBER(s) N00014-82-K-0639
9. PERFORMING ORGANIZATION NAME AND ADDRESS Department of Mechanical Engineering & Mechanics Old Dominion University Norfolk, Virginia 23508		10. PROGRAM ELEMENT, PROJECT, TASK AREA & WORK UNIT NUMBERS Mechanics Division NR 657-694
11. CONTROLLING OFFICE NAME AND ADDRESS Mechanics Division Office of Naval Research Arlington, Virginia 22217		12. REPORT DATE July 1983
		13. NUMBER OF PAGES 84
14. MONITORING AGENCY NAME & ADDRESS (if different from Controlling Office) ONR Scientific Officer Dr. M.M. Reischman		15. SECURITY CLASS. (of this report) Unclassified
		15a. DECLASSIFICATION/DOWNGRADING SCHEDULE
16. DISTRIBUTION STATEMENT (of this Report) This document has been approved for public release; its distribution is unlimited.		
17. DISTRIBUTION STATEMENT (of the abstract entered in Block 20, if different from Report)		
18. SUPPLEMENTARY NOTES		
19. KEY WORDS (Continue on reverse side if necessary and identify by block number)		
20. ABSTRACT (Continue on reverse side if necessary and identify by block number) The root mean square pressure was calculated with synthetically generated pressure signals for transducers of different size. The transducer diameters were in the range of $0.02 < \frac{d}{\delta^*} < 1.18$ at a Reynolds number, Re_{δ^*} , of 12,250. The lower limit of the diameter simulated here was much smaller than diameters reported previously by other workers. Calculated root mean square pressure levels developed in the present work were in good agreement with the measured		

Unclassified

SECURITY CLASSIFICATION OF THIS PAGE (When Data Entered)

Unclassified

SECURITY CLASSIFICATION OF THIS PAGE(When Data Entered)

experimental data.

In order to check the simulated pressure signals, the power spectrum and two point correlation were calculated as well. The power spectra obtained with the smaller transducers were higher in energy level at high frequencies. The shape of the power spectra were similar and overall agreement with experimental data was reasonable. The two point correlations were obtained for separation distances of $\frac{X}{\delta^*} = 1.66$, and 13.37. The same convection and decay effects as the experimental data were observed with the calculated correlations. Again, overall agreement with experimental result was quite good.

Unclassified

SECURITY CLASSIFICATION OF THIS PAGE(When Data Entered)

TABLE OF CONTENTS

	<u>Page</u>
LIST OF FIGURES.....	iii
LIST OF SYMBOLS.....	iv
SUMMARY.....	ix
1. INTRODUCTION.....	1
2. ANALYSIS.....	10
2.1 Transducers with Finite Size.....	10
2.2 Amplification Factor.....	11
2.3 Convection Speed.....	16
2.4 Frequency Cutoff Range.....	17
2.5 Amplitude Decay Function.....	17
2.6 Wavelength Decay Function.....	19
3. RESULTS AND DISCUSSION.....	27
3.1 Two Point Correlation.....	27
3.2 Power Spectra.....	32
3.3 Variation of $P_{R.M.S.}$	41
4. CONCLUSION.....	44
REFERENCES.....	46
APPENDIX A. FORCE CONTRIBUTION OF A SINGLE PRESSURE EVENT.....	48
APPENDIX B. COMPUTER PROGRAM LISTING.....	61

Accession For	
NTIS GRA&I	<input checked="" type="checkbox"/>
DTIC TAB	<input type="checkbox"/>
Unannounced	<input type="checkbox"/>
Justification	
By	
Distribution/	
Availability Codes	
Dist	Avail and/or Special
A	



LIST OF FIGURES

<u>Figure</u>		<u>Page</u>
1	Schematic diagram of the model.....	12
2	Nominal spanwise correlation from Willmarth and Wooldridge (14).....	13
3	Normalized amplitude growth function for a frequency of $\frac{\omega \delta^*}{U_\infty} = 0.205$	15
4	Assumed variation of individual pressure-event convection-velocity with initial frequency.....	17
5	Assumed variation of amplitude with distance for a disturbance with an initial frequency of $\frac{\omega \delta^*}{U_\infty} = 0.205$	20
6	Combined effect of amplification factor and the amplitude decay function on amplitude.....	21
7	Assumed variation of wavelength decay function with distance.....	23
8	Representative simulated pressure fluctuations of upstream reference location.....	24
9	Simulated pressure fluctuations at $\frac{\Delta x}{\delta^*} = 1.66$, shifted in time relative to the reference location via convection speed.....	25
10	Simulated pressure fluctuations at $\frac{\Delta x}{\delta^*} = 13.37$, shifted in time relative to the reference location.....	26
11	Comparison between the auto-correlation function resulting from a simulated wall pressure history and the experimental measurements of Bull [15] for different transducer sizes.....	28
12	Comparison between the two-point correlation function resulting from a simulated wall pressure history and the experimental measurements of Bull [15] for $\frac{\Delta x}{\delta^*} = 1.66$	29
13	Comparison between the two-point correlation function resulting from a simulated wall pressure history	

LIST OF FIGURES (continued)

Figure		Page
	and the experimental measurements of Bull [15] for $\frac{\Delta x}{\delta} = 13.37$ for different transducer sizes.....	30
14	Filtered longitudinal space-time correlations, low-frequency band.....	33
15	Filtered longitudinal space-time correlations, high-frequency band.....	34
16	Narrow bandwidth space-time correlation at spatial separation of $\frac{x}{\delta} = 5$	35
17	Comparison between the power spectrum of a simulated wall pressure history and the experimental measure- ments of Bull [15], Willmarth and Wooldridge [14], and Blake [6]. (Large transducer case).....	37
18	Comparison between the power spectrum of a simulated wall pressure history and the experimental measure- ments of Bull [15], Willmarth and Wooldridge [14], and Blake [6]. (Intermediate transducer case).....	38
19	Comparison between the power spectrum of a sim- ulated wall pressure history and the experimental measurements of Bull [15], Willmarth and Wooldridge [14], and Blake [6]. (Small transducer case).....	39
20	Comparison between the power spectrum of a sim- ulated wall pressure history and the experimental measurements of Bull [15], Willmarth and Wooldridge [14], and Blake [6]. (Ultra small transducer case).....	40
21	Variation of simulated $P_{R.M.S.}$ with transducer size.....	43
A1	A picture of the prototype double sine wave moving over a transducer.....	51
A2	Averaged force as a function of time with a time step smaller than simulation time step (Δt).....	53
A3	Averaged force as a function of time with a time step equal to the simulation time step (Δt).....	55
A4	Temporal resolution of a large wavelength double sine wave with a time step greater than the simulation time step (Δt).....	56
A5	Temporal resolution of a large wavelength double sine wave with a time step equal to the simulation time step (Δt).....	57

LIST OF FIGURES (concluded)

<u>Figure</u>		<u>Page</u>
A6	Temporal resolution of a small wavelength double sine wave with a time step equal to the simulation time step (Δt).....	59
A7	Temporal resolution of a small wavelength double sine wave with a time step smaller than the simulation time step (Δt).....	60

LIST OF SYMBOLS

A	amplitude function
A ₀	original amplitude
a	amplitude decay constant
C _f	skin friction coefficient
d	transducer diameter
d ⁺	Reynolds number dependent transducer size parameter

$$\left(d^+ = \frac{d}{L} \frac{U_\tau}{U_\infty} Re_L \right)$$

f	frequency (Hz)
f _N	Nyquist frequency
f _p	Peak frequency
f _s	Sampling frequency
L	characteristic length
m	wavelength decay constant
n	amplitude decay constant
P(t)	pressure fluctuations
P _{R.M.S.}	Root-Mean-Square Pressure
q _∞	free stream dynamic pressure $\left(\frac{1}{2} \rho U_\infty^2 \right)$

LIST OF SYMBOLS (continued)

Re_L	Reynolds number based on $L \left(\frac{U_\infty L}{\nu} \right)$
Re_δ^*	Reynolds number based on $\delta^* \left(\frac{U_\infty \delta^*}{\nu} \right)$
R_{pp}	space-time correlation
S_t	strouhal number $\left(\frac{\omega \delta^*}{U_\infty} \right)$
t	time
U_∞	free stream velocity
U_c	convection velocity
U_τ	friction velocity $\left(\sqrt{\tau_w / \rho} \right)$
X	coordinate in direction of flow
X_D	development length
X_M	Model length
Z	transverse coordinate

Greek Symbols

α	similarity function $\left(\frac{\omega \xi}{U_c} \right)$
β	similarity function $\left(\frac{\omega \eta}{U_c} \right)$

LIST OF SYMBOLS (concluded)

Greek Symbols (concluded)

Γ	cross-spectral density
γ	wavelength decay constant
δ	boundary layer thickness
δ^*	displacement thickness
η	distance in lateral direction
κ	wavelength decay constant
λ	disturbance wavelength
λ_0	original wavelength
ν	kinematic viscosity
ξ	distance in longitudinal direction
τ	dimensionless time $\left(\frac{U_\infty t}{\delta^*} \right)$
τ_w	wall shear stress
$\phi(\omega)$	power spectral function
ω	radian frequency

EFFECT OF TRANSDUCER SIZE ON THE STATISTICAL PROPERTIES OF
A SIMULATED TURBULENT WALL PRESSURE FIELD

By

Robert L. Ash¹ and Mehdi R. Khorrami²

SUMMARY

The root mean square pressure was calculated with synthetically generated pressure signals for transducers of different size. The transducer diameters were in the range of $0.02 < d < 1.18$ at a Reynolds number, Re_d of 12,250. The lower limit of the diameter simulated here was much smaller than diameters reported previously by other workers. Calculated root mean square pressure levels developed in the present work were in good agreement with the measured experimental data.

In order to check the simulated pressure signals, the power spectrum and two point correlation were calculated as well. The power spectra obtained with the smaller transducers were higher in energy level at high frequencies. The shape of the power spectra were similar and overall agreement with experimental data was reasonable. The two point correlations were obtained for separation distances of $k/\delta = 1.66$, and 13.37. The same convection and decay effects as the experimental data were observed with the calculated correlations. Again, overall agreement with experimental result was quite good.

¹ Eminent Professor, Department of Mechanical Engineering and Mechanics, Old Dominion University, Norfolk, Virginia 23508.

² Graduate Research Assistant, Department of Mechanical Engineering and Mechanics, Old Dominion University, Norfolk, Virginia 23508.

I. INTRODUCTION

Turbulent wall pressure data are required for the analysis of engineering problems related to noise production on aerodynamic bodies, as well as vibration and panel flutter studies (Dowell [1])*. In recent years, the identification of compliant walls which are receptive to turbulent pressure fluctuations has been of particular interest (Bushnell et al. [2] and Buckingham et al. [3]). It has been speculated that a compliant surface might be capable of interacting with a turbulent flow to produce a net drag reduction. When local instantaneous pressure data are required, the resolution capability of even the smallest pressure transducers becomes a serious limitation because they average the pressure field spatially (Corcos [4] and Emmerling, Meir and Dinkelacker [5]). The purpose of this investigation has been to utilize a synthetic pressure field to study the effect of transducer size.

Instantaneous wall pressure fluctuations can be generated either by employing large arrays of pressure transducers with prescribed spatial resolution in an experiment or, by solving the full three-dimensional Navier-Stokes equations. Although, both methods can be more accurate than a simulation, they represent a formidable task in terms of time and expense and are restricted to a particular temporal and spatial resolution. The Monte Carlo technique employed in the present work is capable of resolving arbitrarily in time and space.

The contributions from small scale motions (with length scales on

* The numbers in brackets indicate references.

the order of $\frac{\nu}{U_\tau}$, where U_τ is the friction velocity) to the wall pressure cannot be measured currently because no pressure transducers are sufficiently small. However, during the late sixties and early seventies the importance of high frequency pressure fluctuations on the measurements of root-mean square pressure ($P_{R.M.S.}$) was established by Blake [6] and Emmerling, Meir and Dinkelacker [5] and a rough estimate of their contribution to $P_{R.M.S.}$ was given by Emmerling, Meier and Dinkelacker [5]. The understanding of the above features were made possible by employing pressure transducers which were miniature when compared to earlier experiments. Data generated from these sensors indicated that the R.M.S pressure increased asymptotically with decreasing transducer size. The present work has attempted to clarify the above suggestion by using synthetic pressure fluctuations to study the effect of a controlled, repeatable pressure history on the measurements from different sensor sizes. In order to validate the synthetically generated pressure fluctuations, other important features of a turbulent boundary layer (such as power-spectrum and two point correlation) have been calculated as well.

In recent years, a unified view has evolved concerning the existence of two different scales of disturbances in a turbulent boundary layer. Some disturbances have scales which are comparable to displacement thickness (δ^* , which can be related directly to boundary layer thickness) and other disturbances have much smaller characteristic lengths which are on the order of $\frac{\nu}{U_\tau}$. It is now obvious from the log-log plot of power spectrum, that any shift in the high frequency region due to the measurements of small scale eddies, can result in an increase

in R.M.S. pressure (Blake [6]), since, $P_{R.M.S.}$ is related to the power-spectral density by:

$$\overline{p^2} = 2 \int_0^\infty \Phi(\omega) d\omega.$$

Kraichnan (8) first tried to calculate important features of a pressure field by integrating Poisson's equation

$$\nabla^2 p = -\rho \frac{\partial^2 U_i U_j}{\partial X_i \partial X_j},$$

over a finite region. In a subsequent paper, Kraichnan [9] assumed local isotropy in planes parallel to the surface and used a crude model for mean velocity, to estimate the contribution from turbulent mean shear interactions (which he concluded were the dominant terms). He also assumed that any column of fluid with a length scale comparable to the boundary layer thickness was statistically independent of the adjacent columns. The estimated R.M.S pressure was found to be about six times the wall shear stress. Recent experiments by Emmerling, Meier and Dinkelacker [5] and Bull and Thomas [10] have shown that Kraichnan's $P_{R.M.S.}$ estimate was in good agreement with their measure-considering the degree of approximation he had employed.

Corcos [4] integrated a corrected power-spectrum (his method will be discussed later) and was able only to give the ratio

$$\frac{\overline{p_m^2}}{\overline{p^2}} = 0.61$$

where $\overline{p_m^2}$ is the integrated power spectrum of Willmarth and Wooldridge

[14]. The integration was up to radian frequencies given by $\frac{\omega \delta^*}{U_\infty} = 14.3$, which was the highest measured frequency by Willmarth and Wooldridge [14]. He indicated that the contribution from higher frequency fluctuations might be significant. Emmerling, Meier and Dinkelacker [5] have employed an optical method to evaluate the fluctuation field at the wall. For the sake of comparison, they measured the R.M.S. pressure with microphones mounted flush with the wall. They plotted the variation of non-dimensionalized $P_{R.M.S.}$ with non-dimensionalized transducer diameter and compared them with measurements of several other experiments. Their variables were made dimensionless with respect to free stream dynamic pressure, q_∞ , and inner variables $\frac{v}{U_\tau}$, respectively. Their plot showed a dramatic increase in R.M.S. level as the non-dimensionalized diameter was decreased below $\frac{U_\tau d}{v} = 150$. Emmerling, Meier and Dinkelacker [5] have indicated that when the scaling of transducer diameter was with respect to the displacement thickness, δ^* , the data did not collapse onto a single curve. This suggested that small scale eddies were major contributors to the $P_{R.M.S.}$ (or power spectrum) of a turbulent boundary layer.

In order to understand the results given by Emmerling, Meier and Dinkelacker [5], Bull and Thomas [10] conducted an experiment where direct power-spectral measurements were made using pinhole microphones and piezoelectric transducers with the same diameter. With a similar plot to that of Emmerling, Meier and Dinkelacker [5], they have shown that although there is an increase in $P_{R.M.S.}$ with decreasing diameter,

the increase is not as significant as reported earlier. Bull and Thomas [10] have attributed the high values of $P_{R.M.S.}$ measured by Blake (6) and Emmerling, Meier and Dinkelacker [5] to the local flow disturbances created by the pinhole-microphones.

Recently, Bull and Langeheineken [11] reproduced the experiment of Bull and Thomas [10]. They reinterpreted the transducer size parameter d^+ , which was Reynolds number dependent and given by:

$$d^+ = \frac{d}{L} \frac{U_\tau}{U_\infty} Re_L$$

where L is the characteristic length of the flow field (pipe radius or boundary layer thickness). Their plots of $\sqrt{P^2}/q_\infty$ vs d^+ and Re_L show similar trends for condensor microphones and piezoelectric transducers. Therefore, they concluded that condenser microphones and piezoelectric transducers give essentially identical results (which is contrary to the explanation of Bull and Thomas [10]). However, the above conclusions have produced other questions. Firstly, since the transducer diameters were not equal, direct comparison with Bull and Thomas' [10] results were not possible. Secondly, their experiment was conducted in a pipe flow which raises questions concerning how different flow fields affect the turbulent wall pressure field. Specifically, the question of whether the pressure gradient imposed in a pipe flow alters the statistical properties of the pressure fluctuations must be addressed.

Most of the semi-empirical work concerned with the correction for transducer size has followed the method first outlined by Uberoi and Kovaszny [12]. They developed a mapping procedure based on a knowledge of the instrument response which enabled them to form a response kernel for the measuring system. The original signal (or the instantaneous signal, since they have assumed the instrument response is perfect) could be retained. But, the limitation of their method was due primarily to the assumption of a total random field which was isotropic and homogeneous. The established fact that turbulence has a "fading memory" implies that it is neither homogeneous nor isotropic. Corcos [4] utilized the work of Uberoi and Kovaszny [12] to develop a similarity model for cross-spectral density in the form:

$$\Gamma(\omega, \xi, \eta) = \phi(\omega) \alpha\left(\frac{\omega\xi}{U_c}\right) \beta\left(\frac{\omega\eta}{U_c}\right) e^{-i\omega\xi/U_c}$$

where $\alpha\left(\frac{\omega\xi}{U_c}\right)$ and $\beta\left(\frac{\omega\eta}{U_c}\right)$ are similarity functions (based on the experimental data of Willmarth and Wooldridge [14]) for the longitudinal and lateral directions, respectively. He assumed a uniform response over the transducer surface which had a kernel function equal to the inverse of its area. That form is consistent with the earlier work of Uberoi and Kovaszny [12]. Corcos was then able to show how sensor size influenced resolution for high frequency fluctuations. However, he was not able to give a quantitative estimate for the error.

Willmarth and Roos [13] used an identical procedure with Corcos [4] to show that Corcos's similarity rule was not valid for the high frequency range when the spatial separation between transducers is less

than $0.78 \delta^*$. Willmarth and Wooldridge [14], in their measurements, discarded fluctuations with frequencies less than $\frac{\omega \delta^*}{U_\infty} = 0.14$, because of poor reproducibility of the power spectrum in that range. They have attributed the problem to wind tunnel noise, and propagation of disturbances upstream. Bull's [15] power spectral density has the same drop off and peak frequency as Willmarth and Wooldridge [14] but he was able to make reproducible measurements at frequencies as low as $\frac{\omega \delta^*}{U_\infty} = 0.025$.

Blake [6] used a very small "pinhole" microphone to study the contribution of small scale fluctuations to the power-spectrum. He pointed out that at high frequencies the scaling on outer variables (δ^* and U_∞) was poor. As has been discussed earlier, Bull and Thomas [10] made spectral measurements with two different types of transducers. They found that the high frequency energy content was four times greater when measured with pinhole microphones than when measured with piezoelectric transducers. However, by employing a specially fitted cap, the piezoelectric transducer was converted into a pinhole microphone and the measured power-spectrum was then in close agreement with the spectrum produced by the original pinhole microphone.

Bull and Langeheineken [11] have pointed out the lack of experimental pressure data in low Reynolds number turbulent flows. Their work covered for the first time a wide range of Reynolds numbers in a single experiment. They have shown indeed that the power-spectrum--particularly at high frequencies--is highly Reynolds number dependent. Also, their non-dimensionalization of power-spectra (they have used a variety of dimensionless correlations) suggest that there is no single similar-

ity variable which causes the spectral curves to collapse onto a single curve.

Calculation of auto-correlation, $R_{pp}(\tau)$, is very useful in determination of the time scale over which the pressure fluctuations correlate (along with determination of convection speed and decay of the pressure field). That is, the time scale is indicative of the time interval over which fluctuations "remember" their past; and the pressure correlation is approximately the same as the velocity correlations, because they are determined by the same physical processes. Theoretically (statistically is a better word) it has been understood that any peak in the power spectrum ($\phi(\omega)$) away from the origin would result in negative region of $R_{pp}(\tau)$. However, the reverse does not hold true.

Experimentally (Bull [15] and Blake [6]), it has been proven that there is a peak away from the origin in the power-spectral density; therefore, one must expect certain negative regions for the auto-correlation. Based on his integration, Kraichnan [8] was able to predict that, unlike isotropic turbulence, any turbulent flow with a slight anisotropy will have negative correlation regions for long separation distances. The above suggestion was later confirmed by Bull [15] and Blake [6].

Monte Carlo methods have been used in this study to construct the synthetic pressure distributions. This work is an extension of earlier work by Ash [16] and Ash and Khorrami [17] where detailed accounts of the construction of the computer programs can be found. Consequently, only the major modifications to the previous work have been discussed here.

The work which follows discusses simulation improvements related to individual event construction, amplification factors, amplitude decay, and wavelength decay functions. Subsequently, the statistical measures of the quality of the simulation are presented and discussed. Finally, an interpretation of the transducer size effect on root-mean-square pressure calculations is presented and conclusions have been made.

2. ANALYSIS

2.1 Transducers with Finite Size

The original computer program (Ash [16]) generated pressure as an instantaneous point function rather than the average force which is measured by a transducer of finite area. The distance between adjacent simulation points and the time resolution could be specified by the user, which enabled arbitrary spatial resolvability. However, in order to check the simulation and produce results which could be compared with experimental data, it was necessary to introduce features which allowed the influence of surface area to be studied.

As described in Chap. 1, the finite size and the type of a pressure transducer can create several size effects (Corcos [4] and Bull and Thomas [10]). The frequency resolution of any sensor is related directly to its characteristic diameter, as well as its construction and its sampling time. As the size of a transducer increases, its frequency response decreases. Furthermore, a large sensor causes a severe averaging effect (see appendix A) which can eliminate some pressure features. The averaging effect results in erroneous measurements, and causes an inaccurate representation of the high frequency fluctuations.

With the previous discussion in mind, an array of storage locations (with arbitrarily prescribed size) were substituted for the point locations used in previous simulations. The program has been modified to permit arbitrary specification of "sensor" locations and sizes. The span of the "flat plate" from the front of the first sensor to the back of the last sensor is called the model length. A schematic diagram of

the model is shown in Fig. 1. The development length is the segment ahead of the first sensor location which does not contain a complete simulation history.

The width of the transducer is assumed to be equal to its length (square area). The range of prescribed diameters (here we use the word "diameter" for convenience) is $0.0196 < \frac{d}{\delta^*} < 1.176$. Figure 2 which represents the spanwise or lateral correlation data measured by Willmarth and Wooldridge [14], indicates that the lateral correlation coefficient remains near unity over that diameter range. It has been assumed subsequently that the pressure fluctuations at the center of the sensing element are not affected appreciably by adjacent uncorrelated spanwise fluctuations.

2.2 Amplification Factor

When a constant convection speed of $0.8 U_\infty$ was used in the program, it was found that convection speed calculated from the space-time correlation curves exceeded the free stream velocity; this is obviously inconsistent with every experimental finding. Several different corrections were tested before it was concluded that the problem was caused by the instantaneous creation of low frequency (large wavelength) disturbances. Some of those individual disturbance events were created which spanned more than one simulation location at the instant of creation. These large eddy events would thus have an infinite convection speed. Of course, the number of such disturbances is small compared to the total but, since the low frequency fluctuations decay slowly, the convection speed effect can be pronounced.

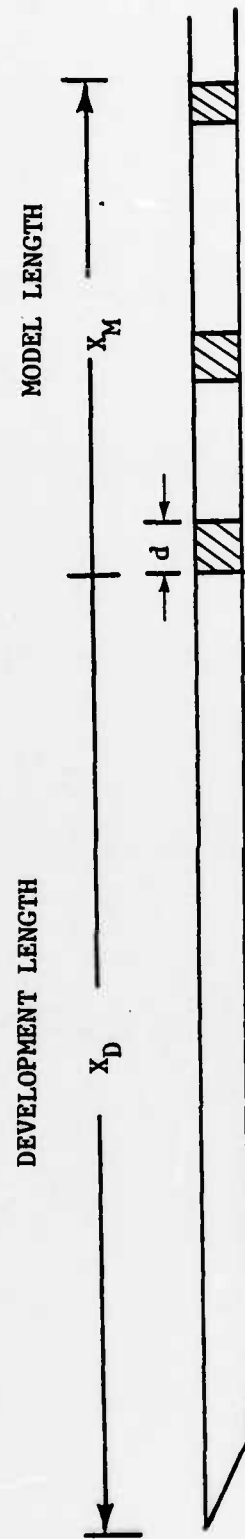


Figure 1. Schematic diagram of the model,
(d is pressure sensing area).

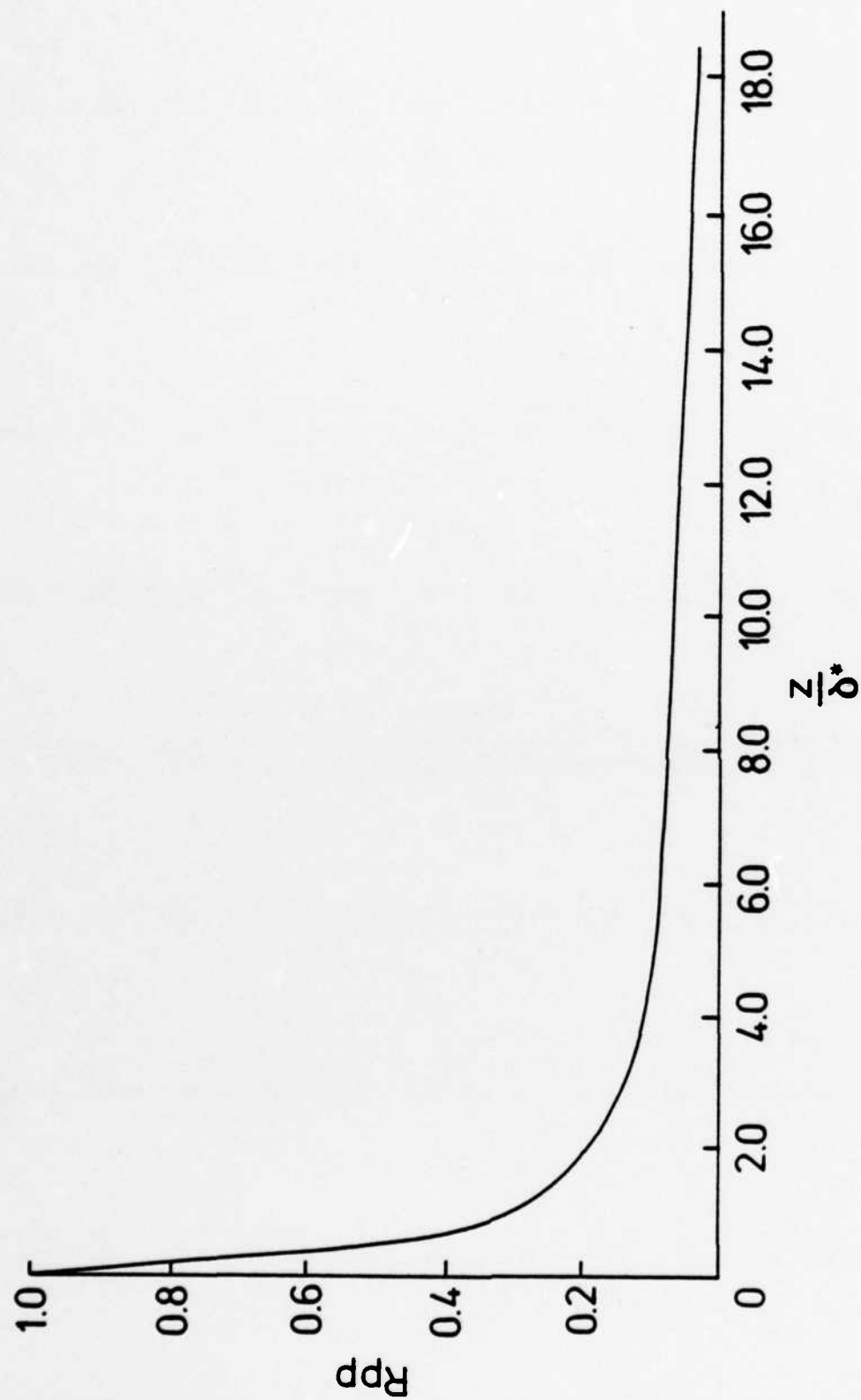


Figure 2. Nominal spanwise correlation from Willmarth and Wooldridge [14].

An amplification time interval has been employed that causes the disturbance amplitude to grow quickly from a small "zero" value to full amplitude, in order to eliminate the infinite convection speed effect. An equation of the form

$$P(x,t) = P_o(x,t) \left[1 - e^{-\frac{4.605t^2}{(\delta^*/U_c)^2}} \right]$$

has been used where $P_o(x,t)$ is the randomly generated event amplitude, U_c is the disturbance convection speed and δ^* is the displacement thickness, while t is the relative time (0 at the instant of generation). Since convection speed is frequency dependent the above growth time interval becomes a larger fraction of the disturbance lifetime for high frequency fluctuations. In fact, at very high frequencies the amplification time can be larger than the decay time, preventing the fluctuation from becoming significant.

Figure 3 shows the plot of the amplification function for a frequency of $\frac{\omega \delta^*}{U_\infty} = 0.205$ which is near the nominal peak frequency. In earlier simulation programs, the amplification function had been non-dimensionalized with respect to boundary layer thickness, δ . However, further testing has shown that δ was not a proper choice. Rather, the displacement thickness, δ^* , scales the simulation results adequately to enable close approximation of a variety of experimental results. Although the amplification procedure caused the simulated convection velocity to decrease below the free stream velocity, the spanning effect due to low frequency disturbances still remained. That is, for short

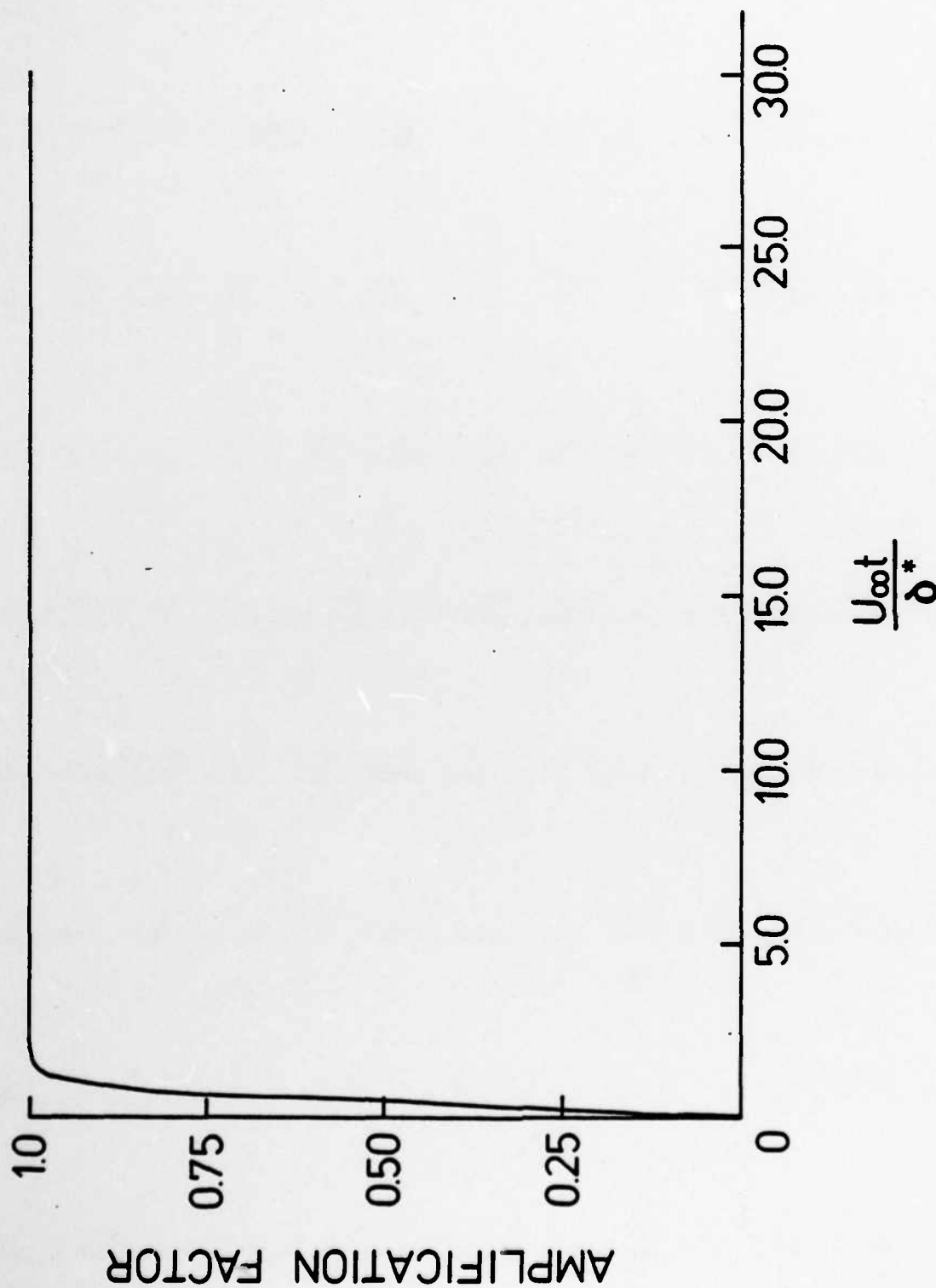


Figure 3. Normalized amplitude growth function for a frequency of $\frac{\omega \delta^*}{U_{\infty}} = 0.205$.

separation distances the convection speed is of order $0.9 U_{\infty}$ compared to an experimental value which is of order $0.6 U_{\infty}$ (even though the assumed event convection speed is on the order of $0.6 U_{\infty}$).

2.3 Convection Speed

Although the constant convection speed of $0.8 U_{\infty}$ gave reasonable results, experiments have shown that wall pressure fluctuations travel downstream with frequency dependent convection speed (5, 15). In order to represent the experimental results more realistically it was necessary to introduce a variable convection speed into the simulation. A problem still remained, because virtually every experimenter has found a different range of convection velocities (see Emmerling, Meier and Dinkelacker [5], Bull [15]). This discrepancy between individual event convection speed and apparent convection speed was most pronounced for the high frequency fluctuations which are normally attributed to near wall effects.

Initially the semi-theoretical convection speed model of Corcos [4] was used to represent the convection velocity. His model assumed an exponential variation in convection speed. However, in order to avoid computational complexity, a linear variation of convection speed with frequency was preferred. Since experimental data were so scattered, the linear assumption was a reasonable compromise between the recent experiments and a simple functional form. The linearized convection speed was assumed to decrease linearly from 78 percent of the free stream velocity at "zero" frequency to a constant 46 percent of the free stream velocity at frequencies greater than or equal to 34 times peak frequency in the power spectrum. The peak frequency has been taken here as $f_p = 0.33 \frac{U_{\infty}}{\delta^*}$

Hz from Bull [15]. The assumed variation of convection speed with frequency is shown in Fig. 4 along with the limited experimental data from Willmarth and Wooldridge [14].

2.4 Frequency Cutoff Range

The upper limit of the frequency range for individual events is determined by economics (in terms of computer time, and memory) and the resolving time step, which in turn is related directly to the peak frequency. However, the lower limit of the frequency was determined from totally different considerations. First, in every experiment the lower frequency fluctuations have been disregarded because of external uncorrelated noise generation (due to vibration of the wind tunnel or the fan). Since the computer does not have this problem, the low frequency limit could be adjusted in agreement with flow physics. The lower limiting frequencies which can be employed in this study create disturbances which have wavelengths on the order of 50δ , and imply significant correlations over very long distances. This is unrealistic in a boundary layer flow. For the particular case considered here, the simulation generates frequencies in the Strouhal number $\frac{(\omega \delta^*)}{U_\infty}$ range of 0.076 to 15.78, where the lowest frequency utilized corresponds to a wavelength of approximately 8δ .

2.5 Amplitude Decay Function

The earlier experiments concerning the pressure fluctuations have revealed that, contrary to the Taylor hypothesis, eddies must decay while they are convected downstream. Experiments by Willmarth and Wooldridge [14] and later by Bull [15] have shown that each disturbance

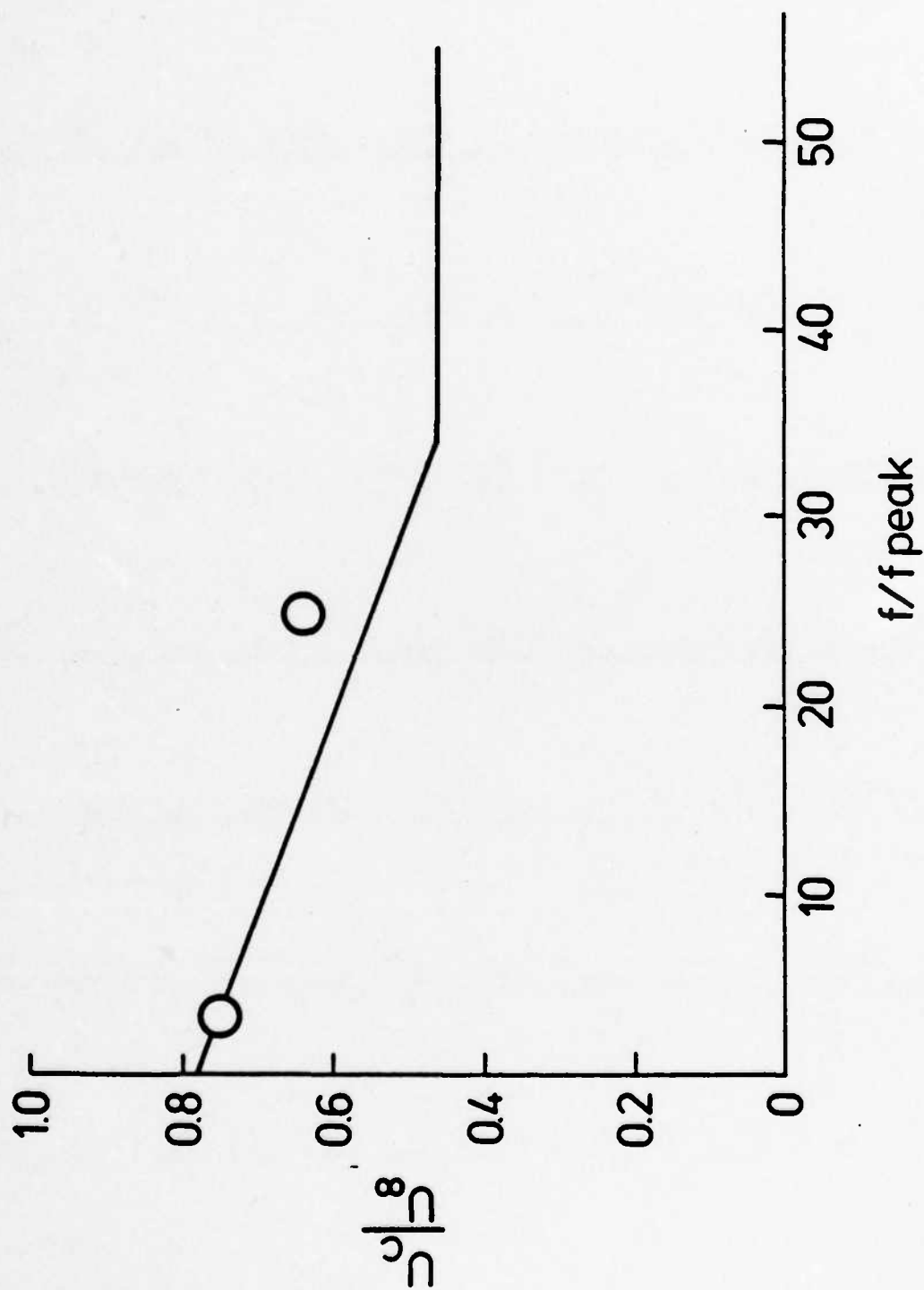


Figure 4. Assumed variation of individual pressure-event convection-velocity with initial frequency.

travels a distance which scales with its wavelength. An amplitude decay function of the form:

$$A(x, \lambda) = A_0 e^{-a(x/\lambda)^n}$$

has been employed where A_0 is the original amplitude, λ is the disturbance wavelength, x is the distance from the point of generation, and a and n are two arbitrary constants, which were determined by trial and error. The constants were specified ultimately by assuming that each disturbance travelled downstream a distance of five wavelengths before it had decayed to one percent of its original amplitude. Figure 5 shows the variation of the decay function with distance for a disturbance with a frequency of $\frac{\omega \delta^*}{U_\infty} = 0.205$. The functional form used here is consistent with the experimental findings of Panton et al. [18] which indicated the initial decay rate is most rapid. Also Fig. 6 shows the combined effect of amplification factor and the decay function on the amplitude.

2.6 Wavelength Decay Function

The three dimensionality of a turbulent boundary layer suggests that the wavelength of a disturbance may change along with its amplitude. This is a very important concept when it is thought of in terms of the power-spectrum and auto correlation. As each disturbance decays in wavelength, the frequency of the disturbance will increase which in turn shifts the peak frequency, along with the power spectrum curve, toward higher frequencies.

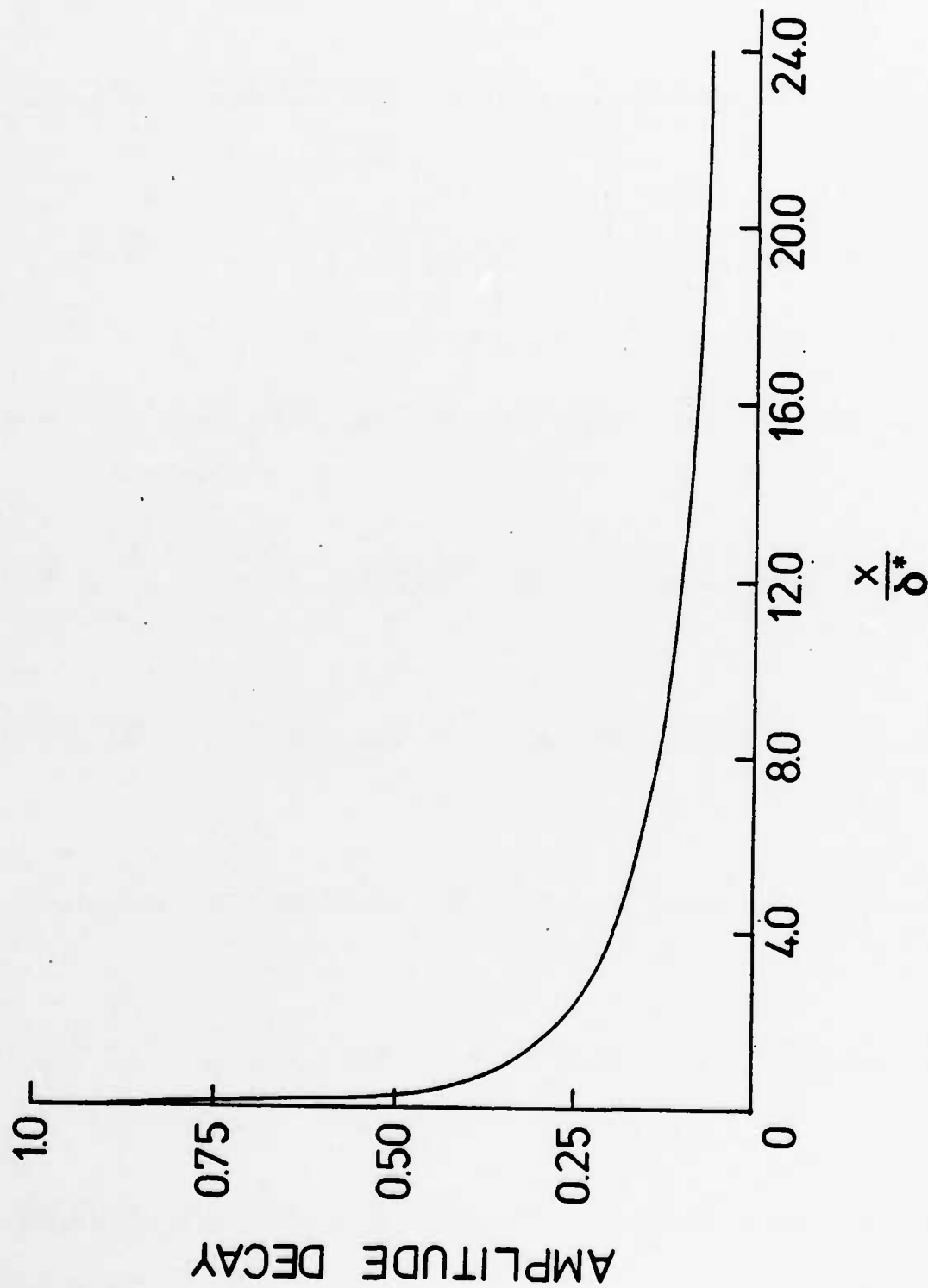


Figure 5. Assumed variation of amplitude with distance for a disturbance with an initial frequency of $\frac{\omega \delta^*}{U_\infty} = 0.205$.

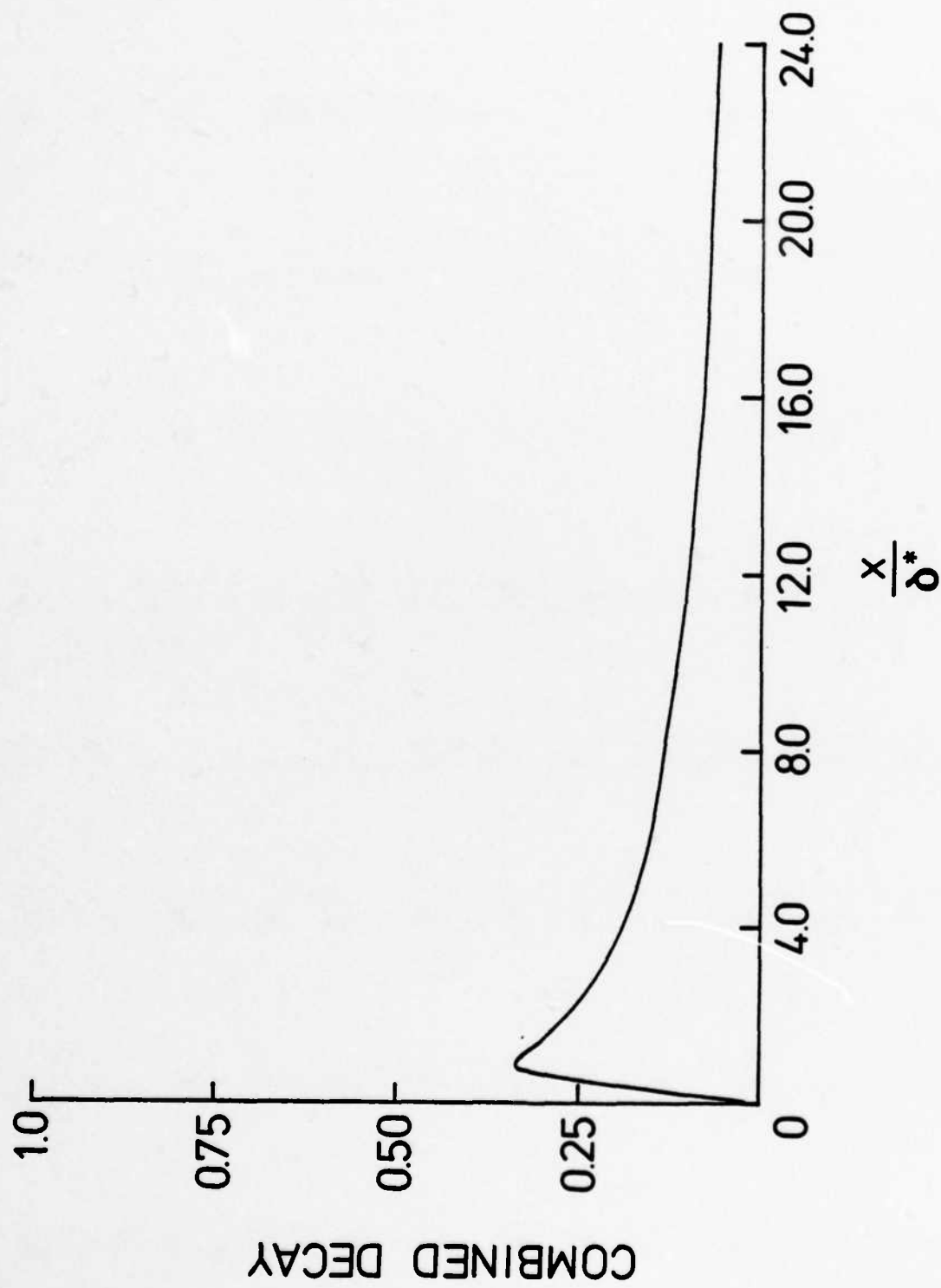


Figure 6. Combined effect of amplification factor and the amplitude decay function on amplitude.

A wavelength decay function of the form

$$\lambda(x) = \lambda_0 [K + D e^{-b(x)^m}]$$

has been used where λ_0 is the original, randomly generated wavelength, K, D, b and m are arbitrary constants which have been adjusted by trial and error. The wavelength decay function allowed the wavelength to be reduced to a specified fraction of its original wavelength at the time of total decay of the disturbance. The wavelength function has improved the simulated auto-correlation but it cannot be considered an optimum function. Figure 7 shows the variation of the wavelength decay function with distance.

In a few cases a frequency dependent decay function similar to the one used for amplitude (see Sec. 2.5) was employed. However, that frequency dependent functional form did not provide any major improvement in simulated statistics but did create some programming difficulty. Therefore, all the runs presented in this work have used a wavelength decay of the form given above.

To make sure that a realistic signal was generated by the simulation, short records of the pressure histories at three different spatial locations have been produced. Those histories are shown in Figs. 8 through 10, and it is obvious that there are recognizable events which have been convected over long distances. However, there are also substantial features which represent "uncorrelated" information. Therefore, it was concluded that the simulated pressure records were similar to actual experimental records.

The program incorporating the modifications described herein is listed in Appendix B.

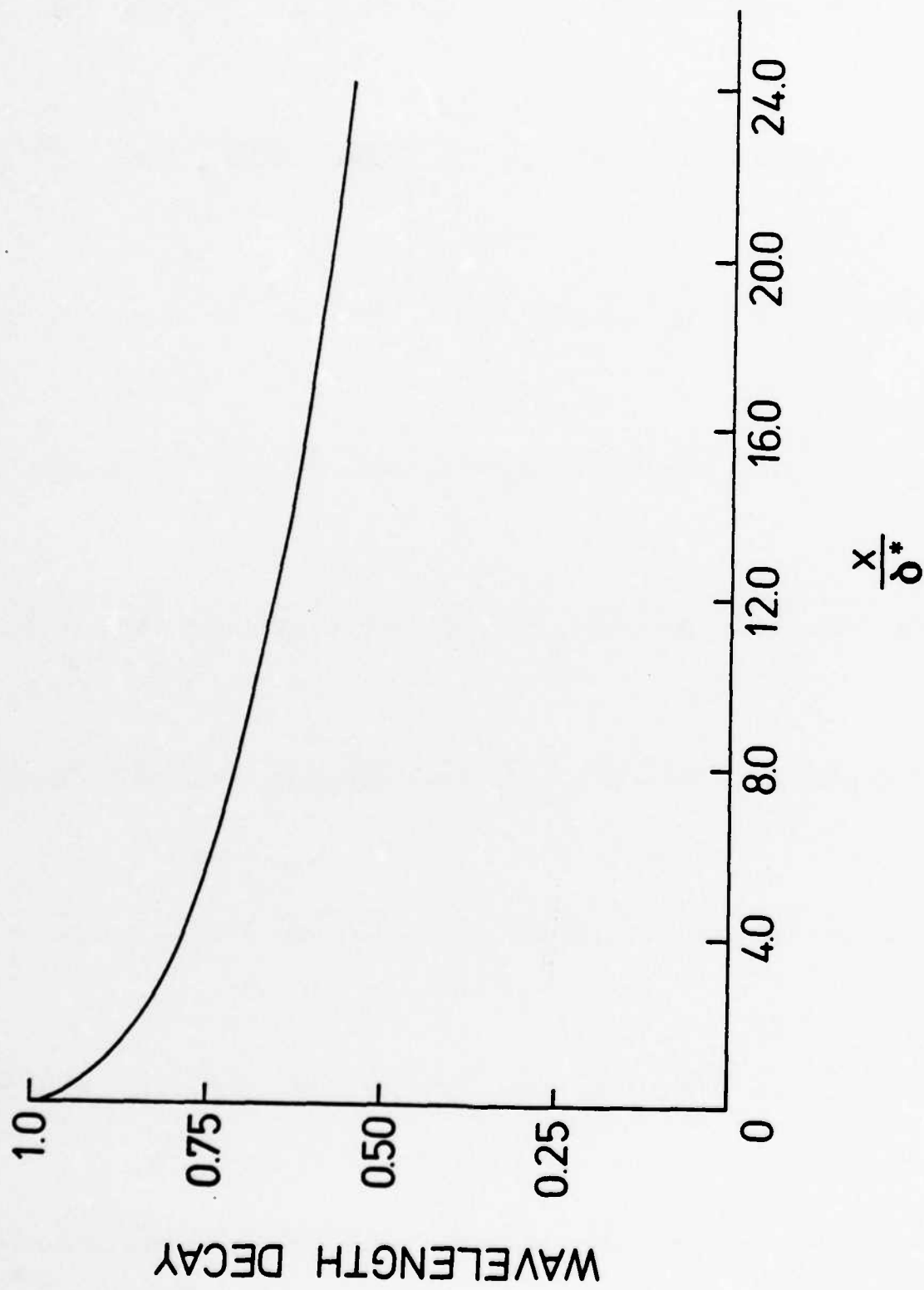


Figure 7. Assumed variation of wavelength decay function with distance.

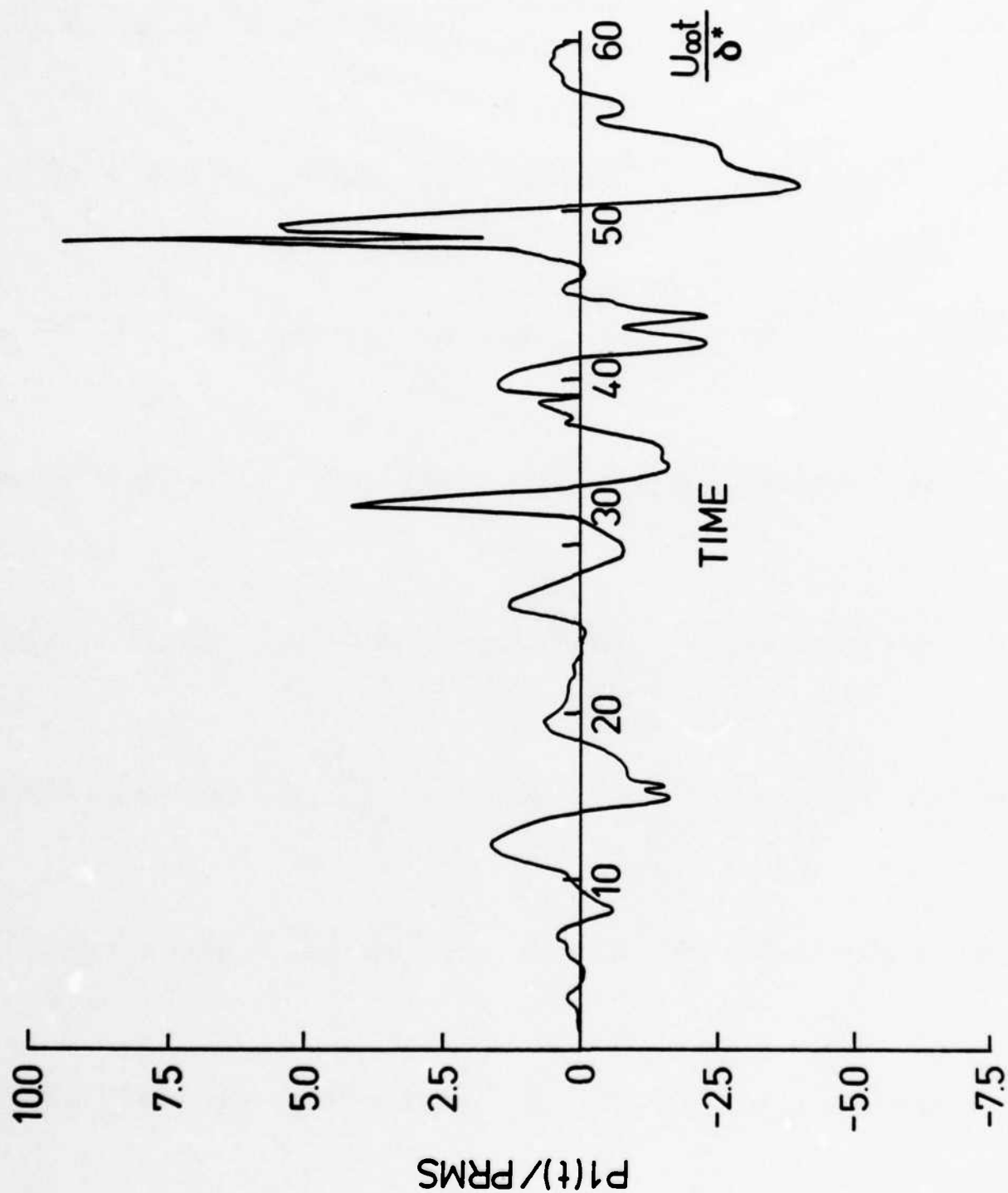


Figure 8. Representative simulated pressure fluctuations at upstream reference location.

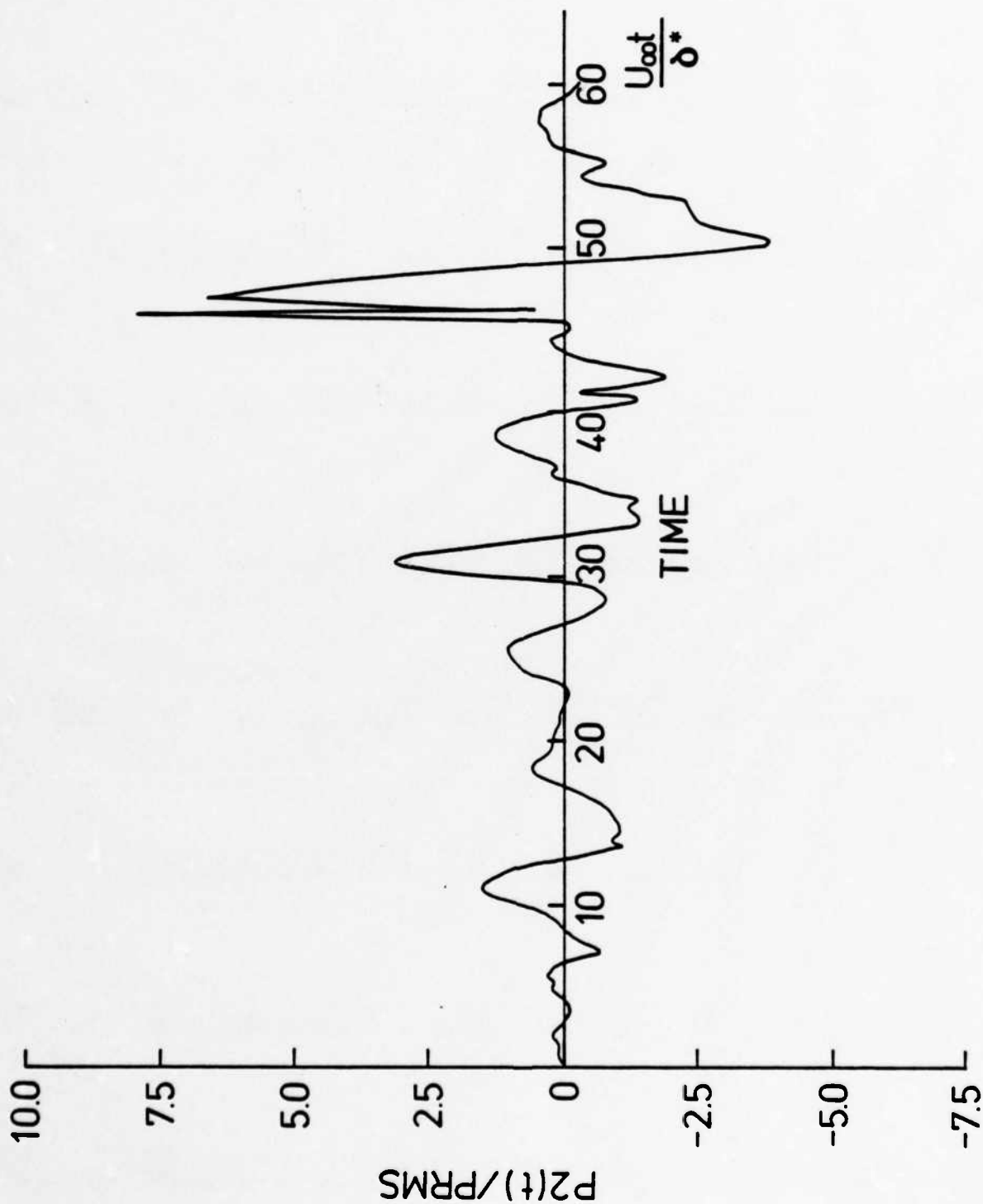


Figure 9. Simulated pressure fluctuations at $\frac{\Delta x}{\delta^*} = 1.66$, shifted in time relative to the reference location via convection speed.

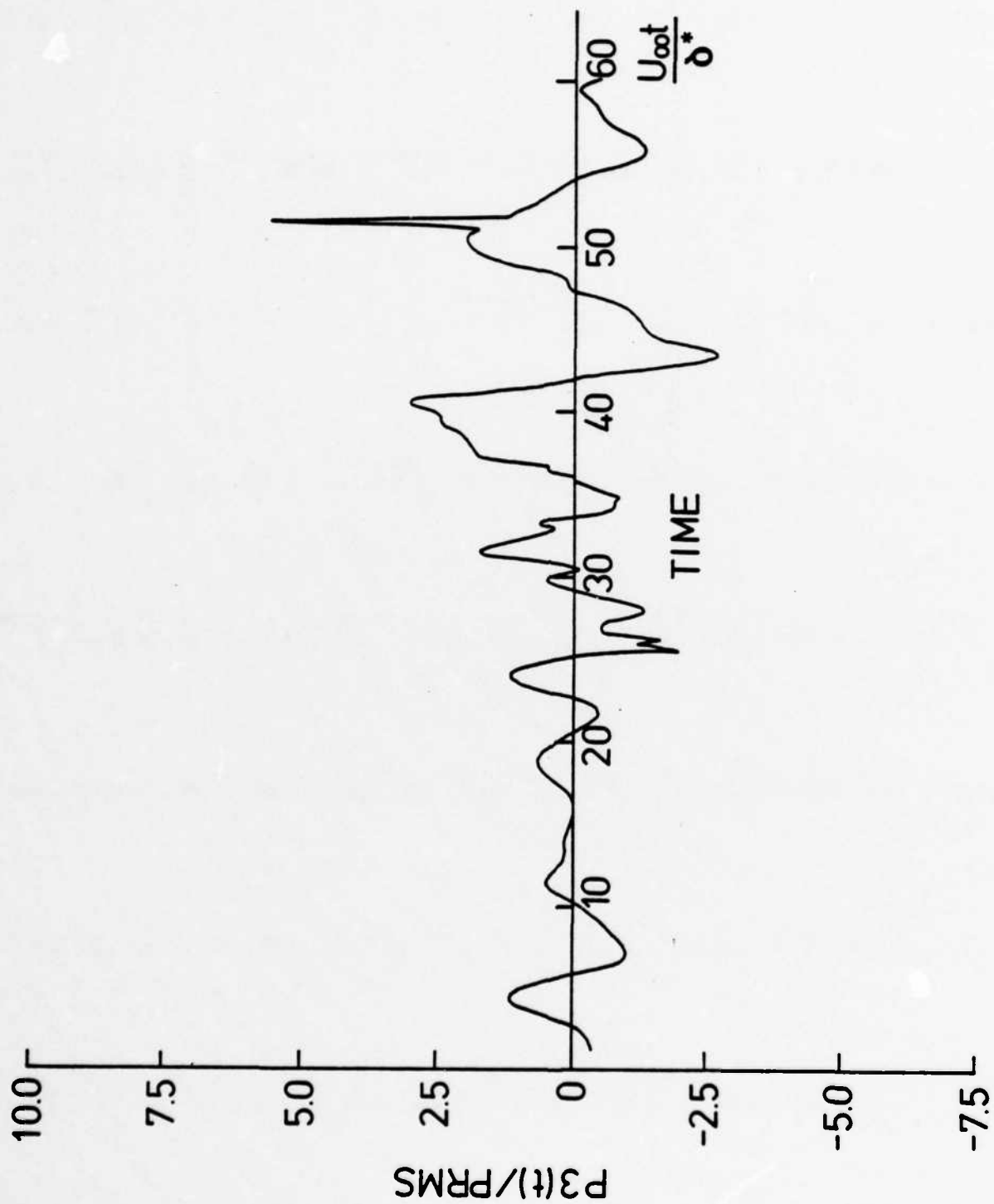


Figure 10. Simulated pressure fluctuations at $\Delta x = 13.37$, shifted in time relative to the reference location.

3. RESULTS AND DISCUSSION

3.1 Two Point Correlation

Two point correlations have been calculated for separation distances, $\frac{x}{\delta^*}$, between 1.66 and 13.37 for a wide range of transducer diameters. The auto-correlation and bounding cases (1.66 and 13.37) are shown in Figs. 11 to 13 along with the experimental data of Bull [15]. Figure 11 shows the auto-correlation at $\frac{x}{\delta^*} = 0$.

It should be noted that the widths of the positive correlation curves become narrower as the transducer diameter is decreased. Note also, that the negative portion of auto-correlation decreases as the diameter is reduced. At the point where $\frac{d}{\delta^*} = 0.0196$, there is an inflection in the auto-correlation (at a dimensionless time delay $\tau=0.3$). The inflection point has been caused by the resolution time step. That is, at the point where $\frac{d}{\delta^*}$ is 0.0196, the time required for many of the simulated pressure events to cross the transducer is smaller than the user specified time step. Hence, the region of large positive correlation is diminished due to the absence of those events.

A phenomenon which is similar to the inflection in the auto-correlation curve can be observed in the two-point correlations for the small separation distance case [$\frac{x}{\delta^*} = 1.66$, Fig. 12] and for the large separation distance case [Fig. 13]. As the transducer size is reduced, it is capable of resolving smaller wavelength disturbances, but those disturbances decay so rapidly that they decorrelate adjacent

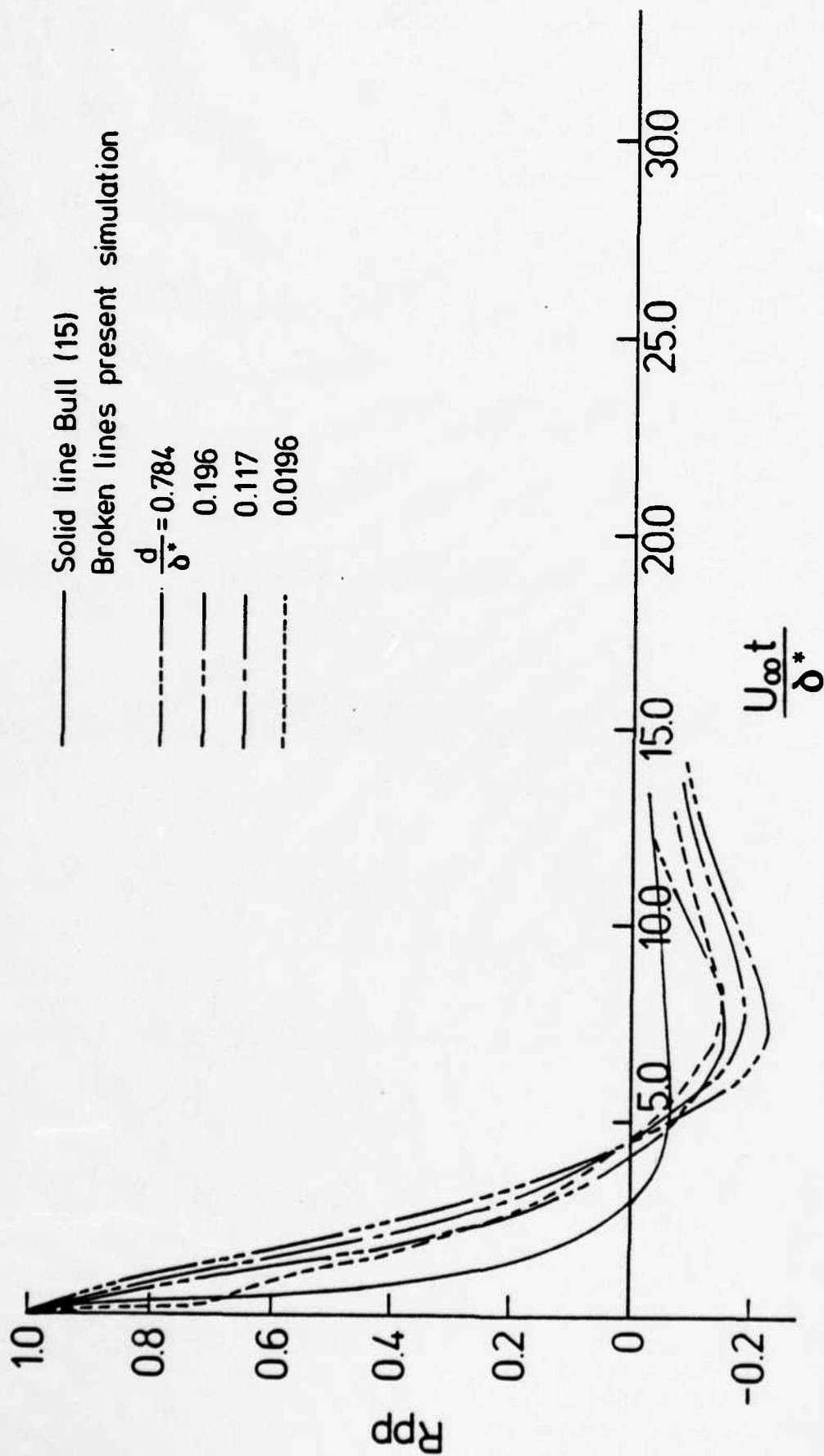


Figure 11. Comparison between the auto-correlation function resulting from a simulated wall pressure history and the experimental measurements of Bull [15] for different transducer sizes.

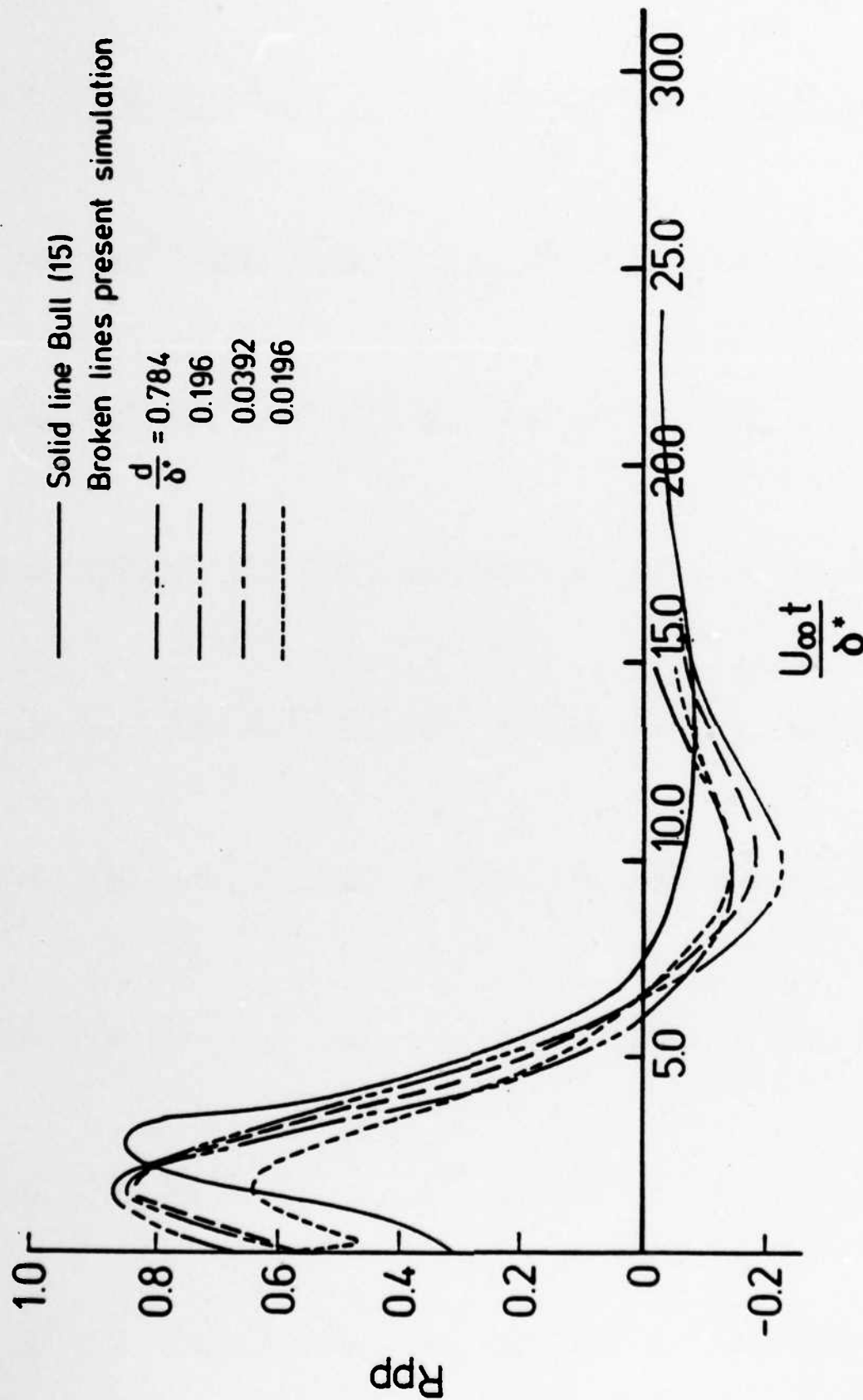


Figure 12. Comparison between the two-point correlation function resulting from a simulated wall pressure history and the experimental measurements of Bull [15] for $\frac{\Delta x}{\delta^*} = 1.66$ for different transducer sizes.

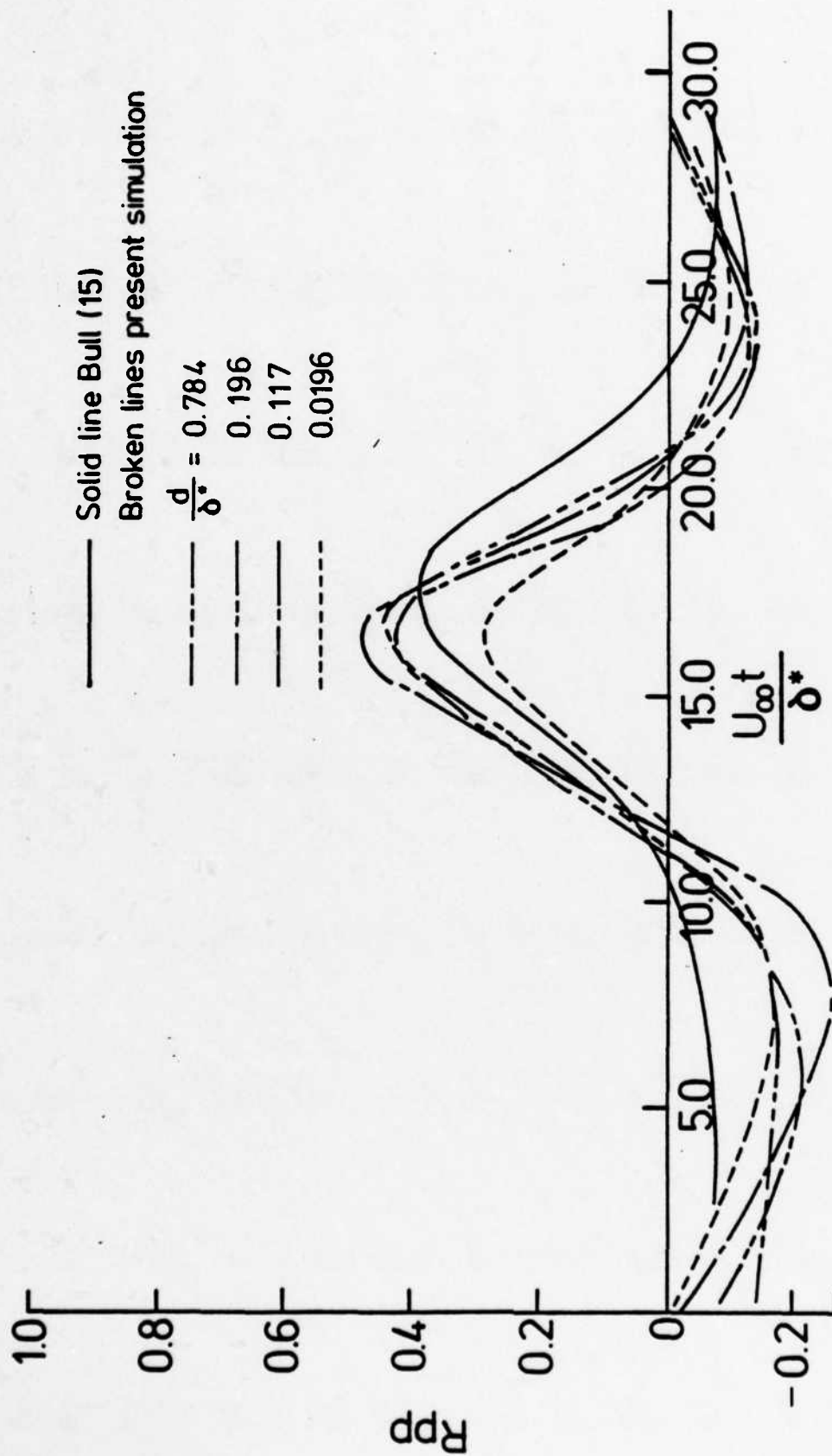


Figure 13. Comparison between the two-point correlation function resulting from a simulated wall pressure history and the experimental measurements of Bull [15] for $\frac{\Delta x}{\delta^*} = 13.37$ for different transducer sizes.

points. Consequently, two-point correlations are reduced as $\frac{d}{\delta^*}$ is decreased below 0.117.

A more subtle effect can also be observed in the two-point correlation data which is due to improved resolution of the low frequency, long wavelength events. For large transducer sizes, a filtering effect is created in the opposite sense to the high frequency case just discussed. The larger transducers cannot resolve and, therefore, are not influenced by the high frequency disturbances. Consequently, the low frequency information is less contaminated and produces a larger correlation coefficient than is actually present. This increased correlation effect is manifested both in an increase in maximum correlation value and an increase in correlation width at a given separation distance.

Finally, for sufficiently large transducer sizes, the measured pressure signal becomes contaminated by the splitting effect discussed in Appendix A. That is, a continuous pressure event is split into two events separated by a "dead band" when the particular pressure event resides entirely upon the transducer. This splitting effect causes a decorrelation to occur between adjacent points which evidently begins for transducer sizes on the order of $\frac{d}{\delta^*} = 0.117$ in this case.

Filtered correlation data have been reported by Willmarth and Wooldridge (14) for pressure signals in the $0.41 < \frac{\omega \delta^*}{U_\infty} < 0.95$ (low band) and $4.1 < \frac{\omega \delta^*}{U_\infty} < 6.8$ (high band) frequency ranges. In order to compare the correlation data produced by the simulation with these results, a pseudo band pass filter has been employed. A comparison can be made by

employing IF STATEMENTS in the simulation program rather than digital filters. That is, only those randomly generated pressure events which had frequencies in the prescribed intervals were allowed to contribute to the transducer histories. Since there are higher harmonics associated with the discrete pressure events, (which were allowed to accumulate using this approach), the "filtering" was not perfect. However, the actual experiments did not employ perfect filters either. The low band and high band data are shown in Figs. 14 and 15 along with the experimental data of Willmarth and Wooldridge (14). In Fig. 15, only the locus curve of the space-time correlation peaks is shown as a solid line. The apparent convection speeds for the simulated case are approximately $0.6 U_{\infty}$ for the high band and $0.8 U_{\infty}$ for the low band.

Narrow band correlation data have also been produced using a similar pseudo filter for a spatial separation of $\frac{x}{\delta^*} = 5.0$. The frequency bands were defined as 16.0 percent on either side of centered frequencies of $\frac{\omega \delta^*}{U_{\infty}} = 0.33, 0.62, 1.15$ and 2.39 and are shown in Fig. 16. The narrow band convection speeds show the proper celerity decrease with increasing frequency. A center frequency of $0.14 \frac{U_{\infty}}{\delta^*}$ was also examined but the correlation results were unsatisfactory for reasons which will be discussed in the next section.

3.2 Power Spectra

Power spectra for the different sized transducer simulations can be developed directly from the auto-correlation data. However, interpreta-

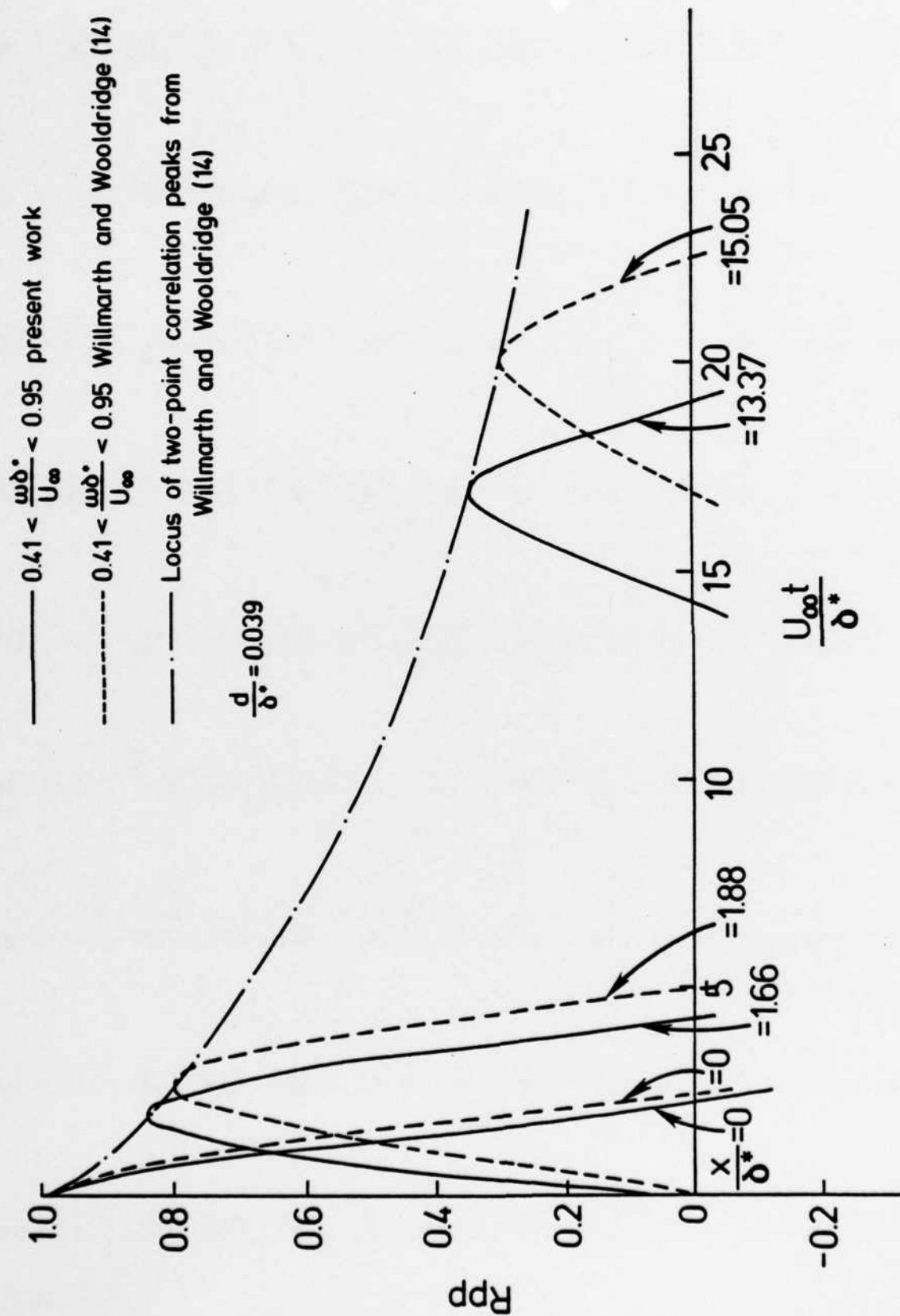


Figure 14. Filtered longitudinal space-time correlations, low-frequency band.

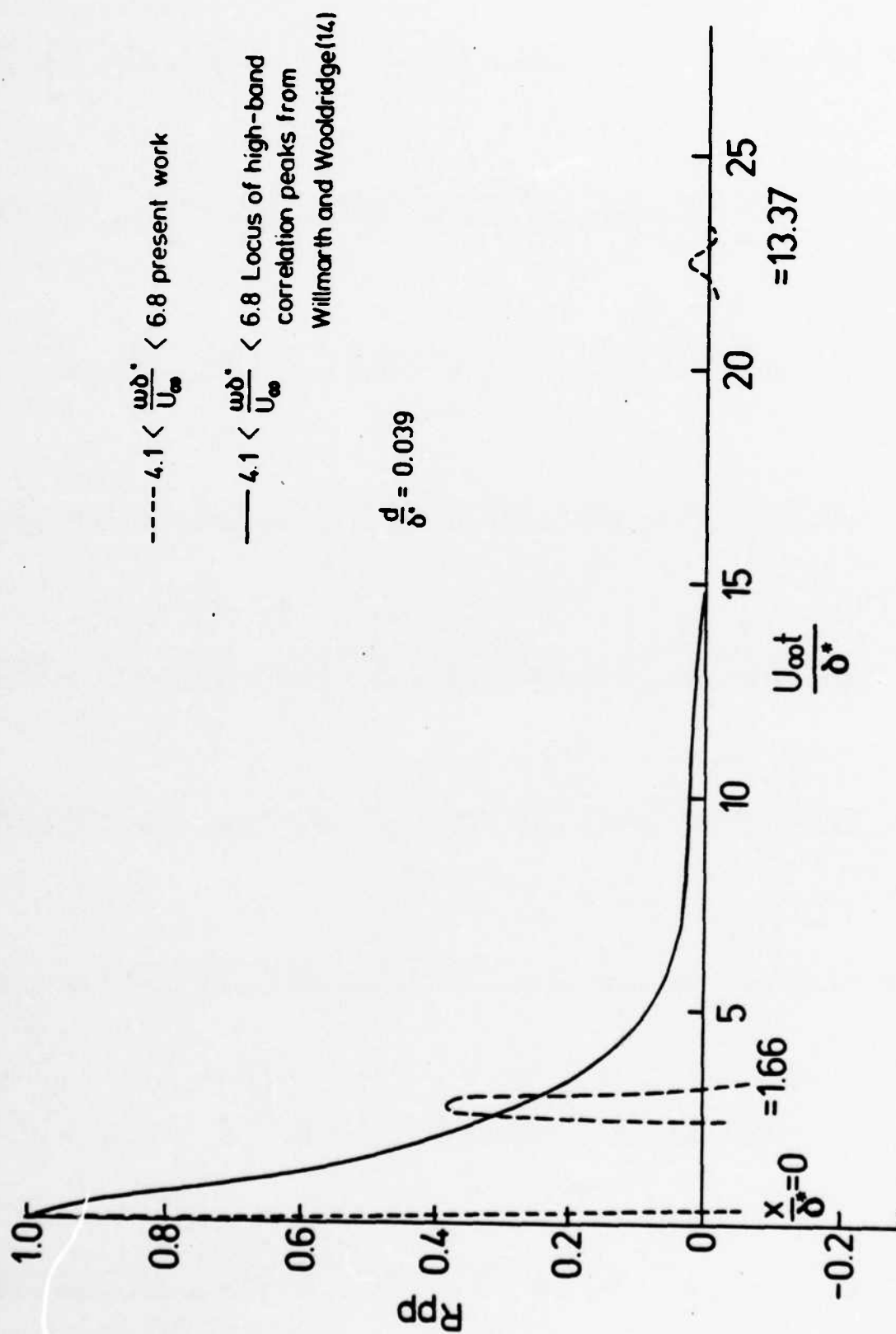


Figure 15. Filtered longitudinal space-time correlations, high-frequency band.

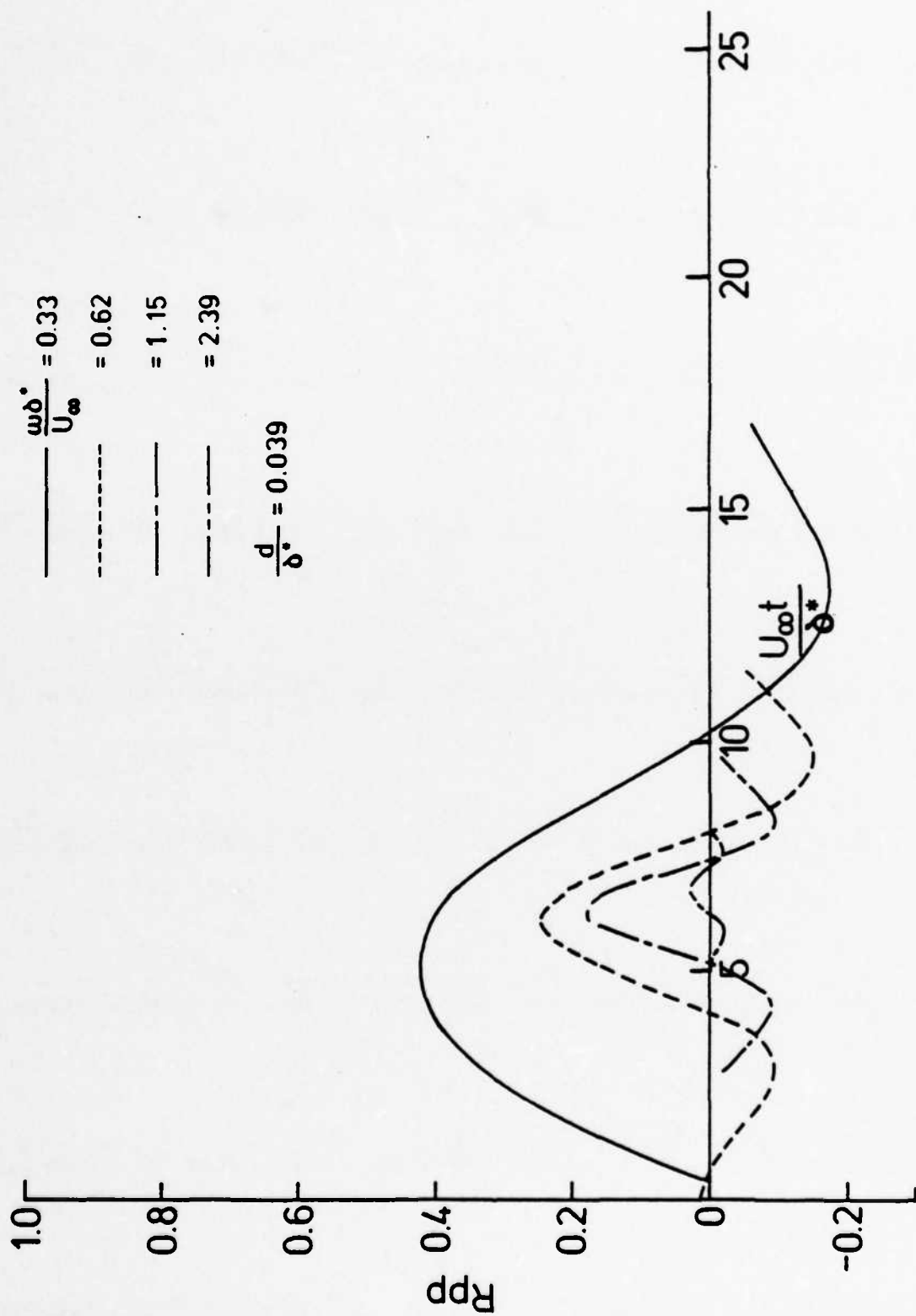


Figure 16. Narrow bandwidth space-time correlations at spatial separation of $\frac{x}{\delta^*} = 5$.

tion of power spectral data is limited to a frequency interval which is controlled by the sampling data (specified time step) and the total time record. Since either a Fourier transform or a fast Fourier transform must be used to extract the power spectrum from the auto-correlation, consideration must be given to the upper frequency limit (Nyquist frequency) where the inverted Fourier transform will begin repeating itself. The sampling frequency f_s must be greater than or equal to $2 f_N$ (where f_N is the Nyquist frequency) in order to be able to recover the original signal from the Fourier transformation.

Figures 17 through 20 represent the variation of power spectra with transducer diameter, where the shaded area is the range of experimental data given by Bull [15], Willmarth and Wooldridge [14], and Blake [6]. The maximum and minimum frequencies generated in the simulation are

$$f_{\max} < \frac{1}{\Delta t}$$

where Δt is the resolving time step and

$$f_{\min} > \frac{1}{T}$$

where T is the total record time. The above maximum frequency generated by the simulation is smaller than the sampling frequency f_s associated with Nyquist frequency f_N of turbulent wall pressure fluctuations. Therefore, the discrepancies between the experimental data and the simulated spectra at the high- and low-frequency extremes are due to the time step resolution and the shortness of the simulated record, respectively. However, the results are in close agreement with the experimental data in the mid-frequency range for a wide variety of diameters. The above figures indicate a small increase in the power level at high frequencies as the diameter approaches zero. Considering

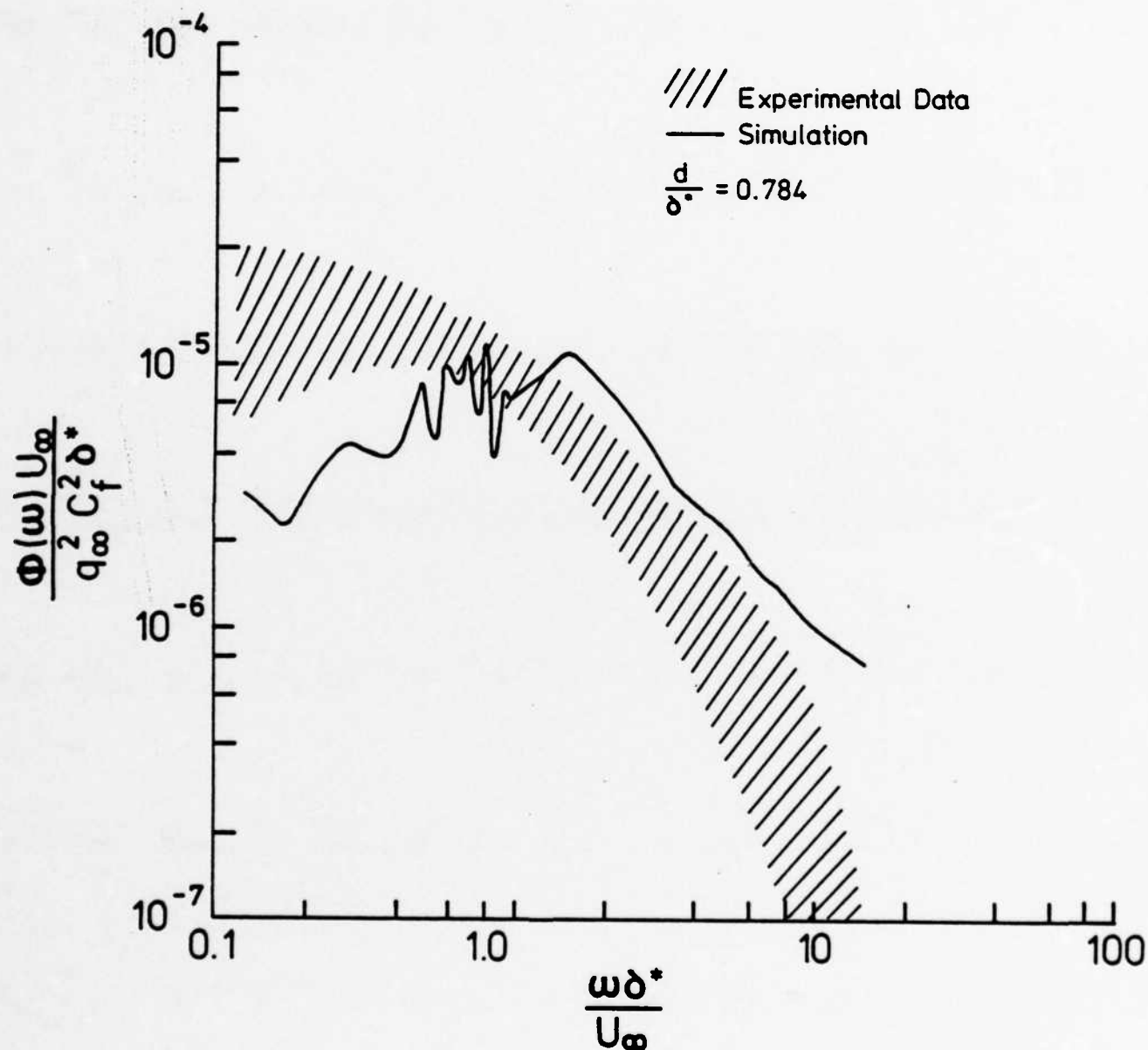


Figure 17. Comparison between the power spectrum of a simulated wall pressure history and the experimental measurements of Bull [15], Willmarth and Wooldridge [14], and Blake [16]. (Large transducer case)

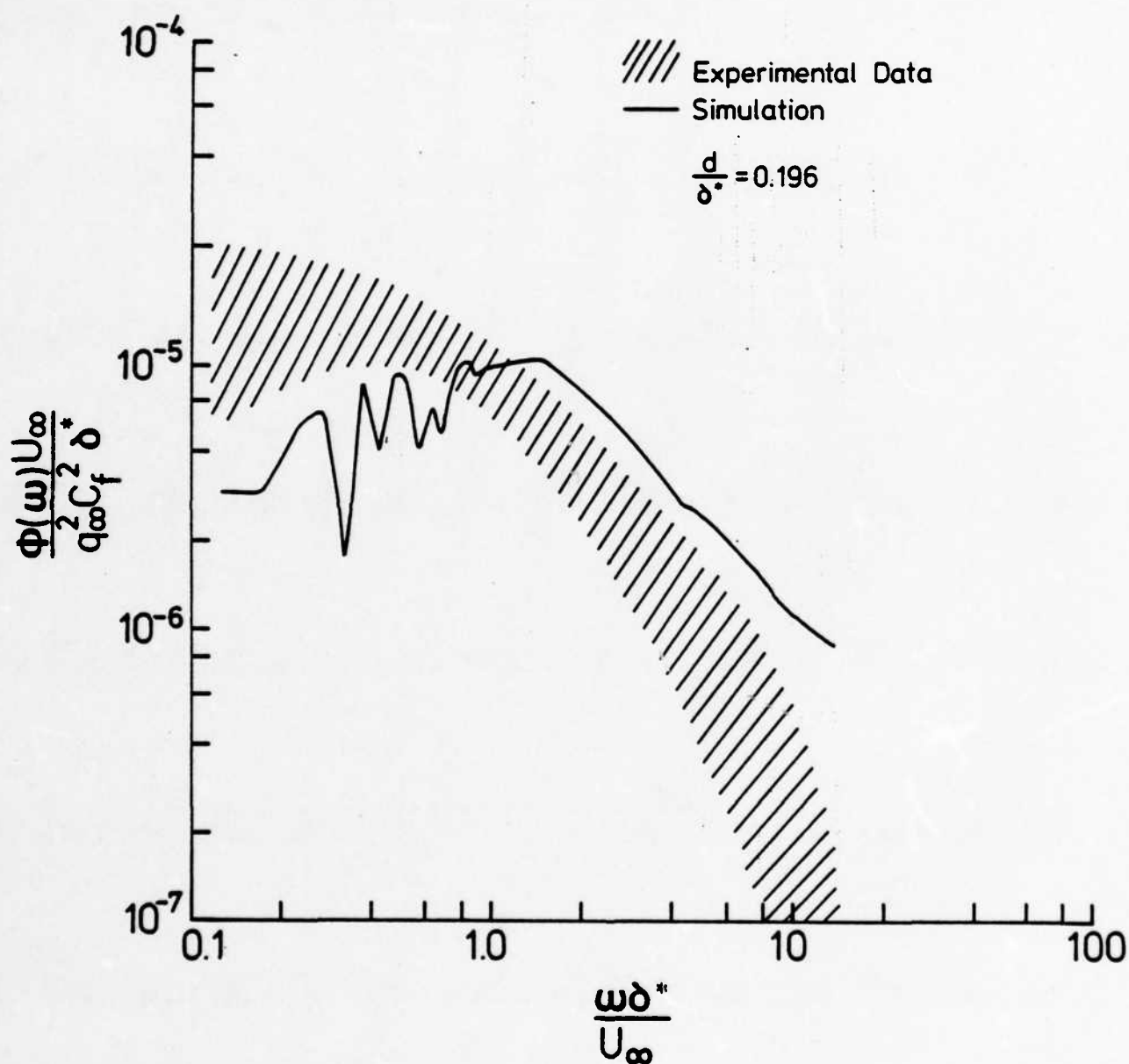


Figure 18. Comparison between the power spectrum of a simulated wall pressure history and the experimental measurements of Bull [15], Willmarth and Wooldridge [14], and Blake [6]. (Intermediate transducer case)

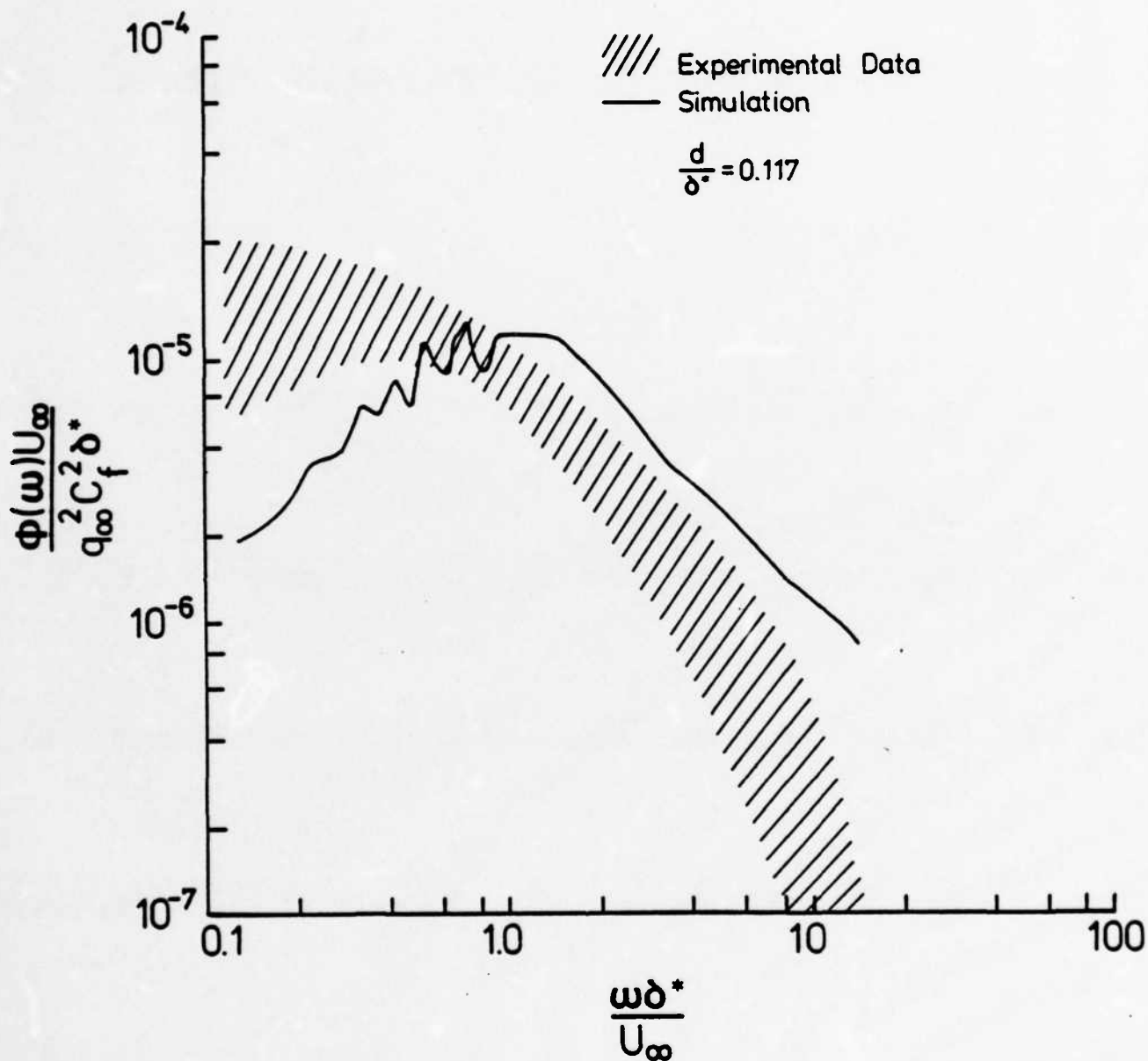


Figure 19. Comparison between the power spectrum of a simulated wall pressure history and the experimental measurements of Bull [15], Willmarth and Wooldridge [14], and Blake [6]. (Small transducer case)

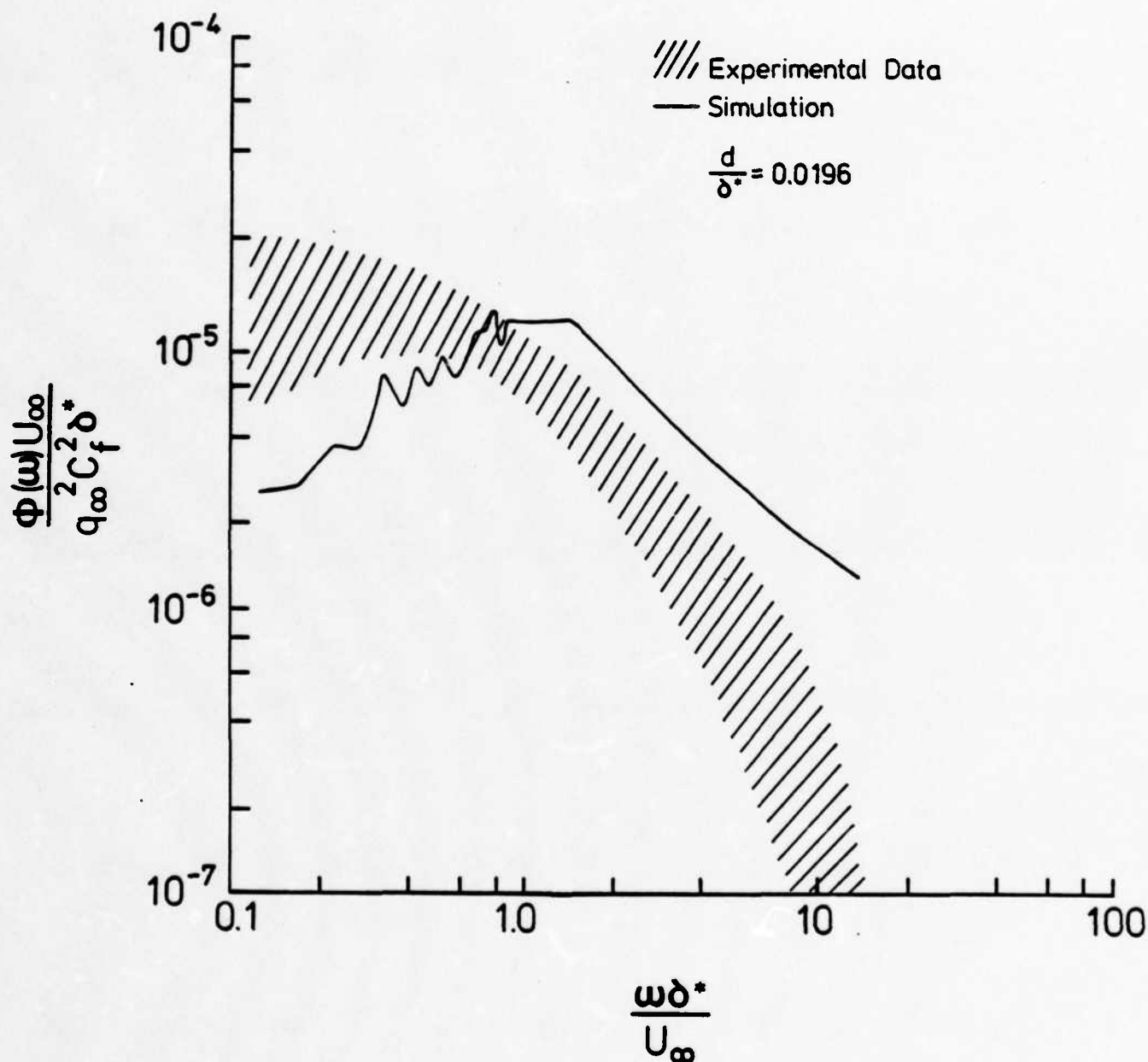


Figure 20. Comparison between the power spectrum of a simulated wall pressure history and the experimental measurements of Bull [15], Willmarth and Wooldridge [14], and Blake [6]. (Ultra small transducer case)

the degree of approximation used in the present work and the scattering of experimental data the agreement between the simulation and experimental results is considered satisfactory.

3.3 Variation of $P_{R.M.S.}$

For many years experimenters scaled transducer diameter data with the boundary layer displacement thickness δ^* [13-15] and showed only small variations of $P_{R.M.S.}$ as the parameter $\frac{d}{\delta^*}$ approached zero. However, more recent results suggest that small scale pressure fluctuations in turbulent boundary layers may have a significant effect on the $P_{R.M.S.}$ value (Blake [6], Emerling, Meier and Dinkelacker [5], and Bull and Thomas [10]). Since most of these high frequency fluctuations are produced in the wall region, it was suggested by Emerling, Meier and Dinkelacker [5] that the scaling of transducer diameter should be with respect to the inner variable $\frac{v}{U_\tau}$ which expands the lower limiting region significantly. They also suggested that instead of wall shear stress, free stream dynamic pressure should be used in normalizing the R.M.S. pressure.

For the present study, it was decided to concentrate numerical testing in the range $\frac{U_\tau d}{v} < 200$, in order to verify the above suggestion. Therefore, diameters with the value $\frac{U_\tau d}{v} = 9, 18, 35, 54, 72, 90, 135, 180, 271, 360, 451, \text{ and } 541$ have been used for testing. The amplitude of $P_{R.M.S.}$ can be adjusted in this simulation by simply changing a scaling parameter in the program. However, an adjustment was made only for one large diameter case to establish a realistic level for use with

all other cases. Hence, each subsequent case was subjected to an identical simulated pressure history. Figure 21 shows the variation of $P_{R.M.S.}$ with the transducer size as measured by Emmerling, Meier and Dinkelacker [5] and Bull and Thomas [10] along with the present simulation results. Although there is a fluctuation of $P_{R.M.S.}$ values for $\frac{U d}{\tau} > 200$, the oscillation is small and $P_{R.M.S.}$ can be represented by a straight line for large diameters. The constant simulated $P_{R.M.S.}$ region is also followed by a sharp increase in the R.M.S. value as the diameter shrinks. The simulated variation approximates the curve given by Bull and Thomas [10].

Although the increase in $P_{R.M.S.}$ is significant, it was not clear whether the jump was caused by the inclusion of high frequency disturbances or by achieving a better resolvability of large disturbances at small diameters. Therefore, a simulation was conducted in which all the disturbance events with wavelengths smaller than $\frac{U \lambda}{\tau} = 180$ were excluded from the simulation. The remaining fluctuations were resolved with a diameter of $\frac{U d}{\tau} = 18$ which is in the range of increased $P_{R.M.S.}$. That test produced the same $P_{R.M.S.}$ and has indicated that very high frequency pressure fluctuations do not contribute measurably to the R.M.S. level.

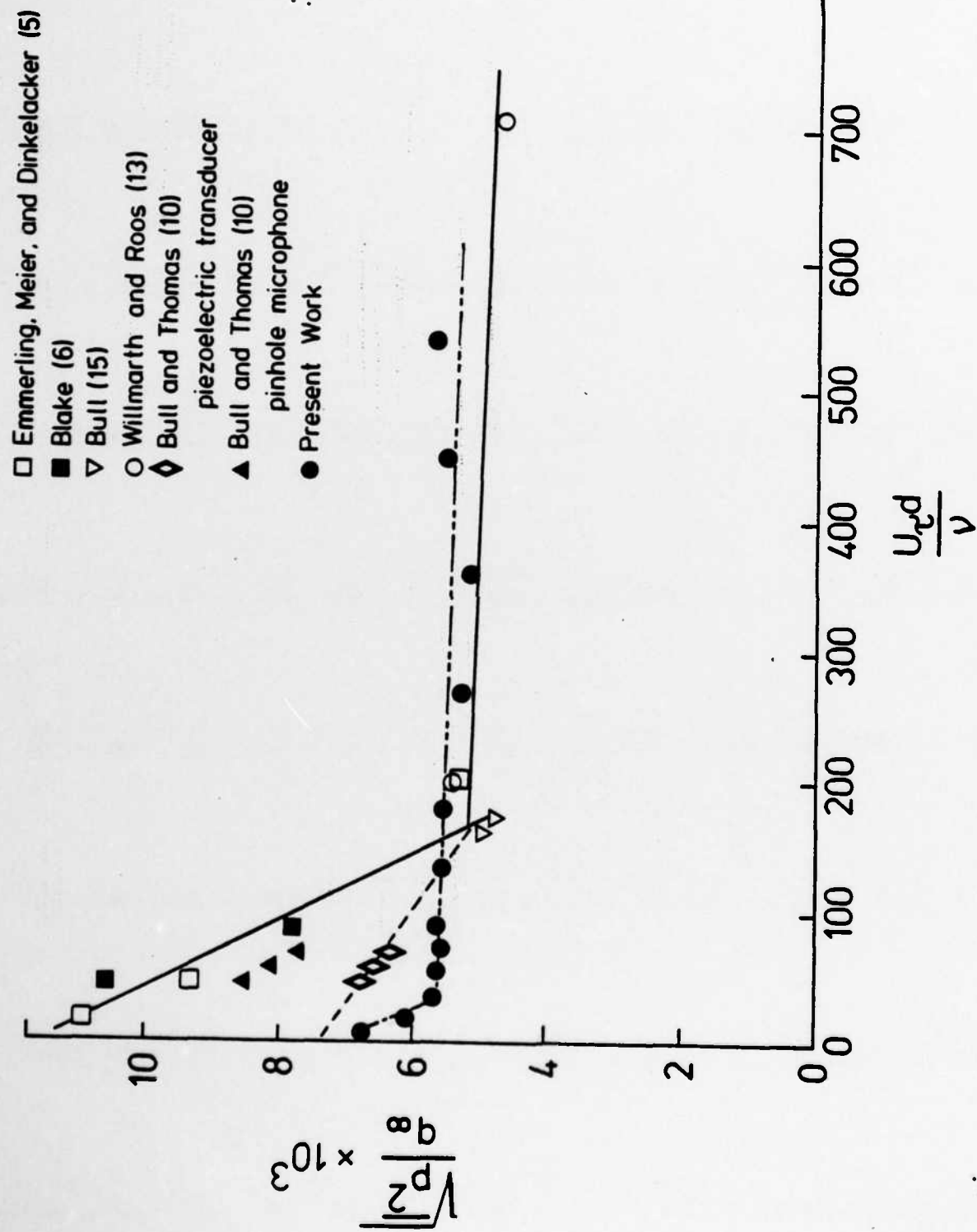


Figure 21. Variation of simulated $P_{R.M.S.}$ with transducer size.

4. CONCLUSION

A wide range of transducer diameters have been used in the present simulation to study the variation of R.M.S. pressure with sensor size when the transducers are exposed to identical signals. It has been shown that the $P_{R.M.S.}$ level increases moderately at small values of $\frac{U_\tau d}{\nu}$ which is consistent with more recent experimental data. The simulated result indicates that $P_{R.M.S.}$ increases from a nominally constant value for sensor sizes smaller than $\frac{U_\tau d}{\nu} \approx 40$ which differs from the departure point of $\frac{U_\tau d}{\nu} \approx 170$ suggested by the experimental data. The simulated curve closely approximates the result given by Bull and Thomas [10] in terms of the magnitude of increase.

Although the rise in the R.M.S. level is significant, the resulting curve suggests that the increase is not as large as that reported earlier by Emmerling, Meier and Dinkelacker [5]. It is known that the above contribution to $P_{R.M.S.}$ has been attributed to small scale structures in the inner region of the turbulent boundary layer by several workers in the field. However, the R.M.S. level of the simulated signal which deleted high frequency events indicated that the contribution of small scale fluctuations to the $P_{R.M.S.}$ is insignificant.

Power-spectra have been calculated for several different transducer diameters. The power spectra showed slight increases in energy content at high frequencies and a slight increase in the peak frequency as the diameter was reduced. The shapes of the spectra are very similar, and the agreement with experimental data is reasonably good.

Two point correlations have been calculated for separation distances of $\frac{x}{\delta^*} = 1.66$, and 13.37. The correlations show clearly the convection and decay patterns of the pressure field. For large transducer diameters the width of the correlation curves increases. This is in accordance with the expectation that higher correlation is obtained when the resolvability of small scale structures is poor. As the diameter is reduced the correlation curves become narrower. Again this is expected since, the inclusion of small pressure fluctuations which do not correlate over large separation distances or time delays, have a significant decorrelation effect. Low- and high-frequency band correlation of the generated pressure fluctuations also showed the correct convection speeds. The narrow band, two point correlations showed a decreasing convection speed as the center frequency was increased. Overall the agreement between the simulated curves and the experimental data of Bull [15] and Willmarth and Wooldridge [14] is quite good.

In summary, we have shown that a simulated turbulent wall pressure signal with properties similar to experimental measurements produces root mean square pressure levels which vary with sensor size in a manner which is similar to experiment. The size effect is not pronounced for the power spectra, but the interesting result that the maximum values of two-point correlations decrease with decreasing size was observed. This effect can be attributed to the increasing contribution from small wavelength pressure fluctuations.

REFERENCES

1. Dowell, E. HJ., "Panel Flutter: A Review of the Aeroelectric Stability of Plates and Shells," AIAA Journal, Vol. 8, No. 3, pp. 385-405, March 1970.
2. Bushnell, D. M., Hefner, H. N., and Ash, R. L., "Compliant Wall Drag Reduction for Turbulent Boundary Layers," Physics of Fluids, Vol. 20, No. 10, Pt. 2, 1977, pp. 33-48.
3. Buckingham, A. C., Chun, R. C., Ash, R. L., and Khorrami, M. M., "Compliant Material Coating Response to a Turbulent Boundary Layer," AIAA Paper No. 82-1027, June 1982.
4. Corcos, G. M., "Resolution of Pressure in Turbulence," Journal of Acoustical Society of America, Vol. 35, No. 2, February 1963, pp. 192-199.
5. Emmerling, R., Meier, G. E., and Dinkelacker, A., "Investigation of the Instantaneous Structure of the Wall Pressure Under a Turbulent Boundary Layer Flow," AGARD Conference Proceedings, No. 131 on Noise Mechanisms, Paper No. 24, 1973.
6. Blake, W. K., "Turbulent Boundary Layer Wall Pressure Fluctuations on Smooth and Rough Walls," Journal of Fluid Mechanics, Vol. 44, Pt. 4, December 1970, pp. 637-660.
7. Bradshaw, P., "Inactive Motion and Pressure Fluctuations in Turbulent Boundary Layers," Journal of Fluid Mechanics, Vol. 30, Pt. 2, November 1967, pp. 241-258.
8. Kraichnan, R. H., "Pressure Field within Homogeneous Anisotropic Turbulence," Journal of Acoustical Society of America, Vol. 28, No. 1, January 1956, pp. 64-72.
9. Kraichnan, R. H., "Pressure Fluctuations in Turbulent Flow Over a Flat Plate," Journal of Acoustical Society of America, Vol. 28, No. 3, May 1956, pp. 378-390.
10. Bull, M. K. and Thomas, A. S. W., "High Frequency Wall Pressure Fluctuations in Turbulent Boundary Layers," Physics of Fluids, Vol. 19, No. 4, April 1976, pp. 597-599.
11. Bull, M. K. and Langeheineken, T., "On the Wall Pressure Field in Turbulent Pipe Flow," Max-Planck-für strömungsforschung, Göttingen, Report No. MPIS-MITT-73, 1981.
12. Uberoi, M. S. and Kovasznay, L. S. G., "On Mapping and Measurement of Random Fields," Quarterly of Applied Mathematics, Vol. 10, No. 4, January 1953, pp. 375-393.

13. Willmarth, W. W. and Roos, F. W., "Resolution and Structure of the Wall Pressure Field Beneath a Turbulent Boundary Layer," Journal of Fluid Mechanics, Vol. 22, Pt. 1, May 1965, pp. 81-94.
14. Willmarth, W. W. and Wooldridge, C. E., "Measurements of the Fluctuating Pressure at the Wall Beneath a Thick Turbulent Boundary Layer," Journal of Fluid Mechanics, Vol. 14, Pt. 2, October 1962, pp. 187-210.
15. Bull, M. K., "Wall Pressure Fluctuations Associated with Sub-Sonic Turbulent Boundary Layer Flow," Journal of Fluid Mechanics, Vol. 28, Pt. 4, June 1967, pp. 719-754.
16. Ash, R. L., "Simulation of Turbulent Wall Pressure," NASA Contractor Report 2958, May 1978.
17. Ash, R. L and Khorrami, M. M., "Simulation of Turbulent Wall Pressure Fluctuations for Flexible Surface Response Studies," AIAA Paper No. 83-0292, January 1983.
18. Panton, R. L., Goldman, A. L., Lowery, R. L., and Reischman, M. M., "Low-Frequency Pressure Fluctuations in Axisymmetric Turbulent Boundary Layers," Journal of Fluid Mechanics, Vol. 97, Pt. 2, March 1980, pp. 299-319.

APPENDIX A

FORCE CONTRIBUTION OF A SINGLE PRESSURE EVENT

The streamwise length of the transducer (size) and the sampling rate (time step) both distort the recorded pressure signal. Depending on the wavelength (and frequency) of the particular fluctuation event, the net pressure contribution sensed by a transducer can vanish even though the disturbance is over the transducer. Also, if sampling rates are slow, an event may be convected completely across the transducer in less than one time step. In order to understand the distortion produced by finite pressure transducers and sampling rates, calculations have been made for a variety of prototype pressure events, $\Delta P(x,t)$, given by:

$$\Delta P(x,t) = \begin{cases} 0 & , \quad x < ct-L \\ \sin \frac{2\pi(x-ct)}{L} - 1/2 \sin \frac{4\pi(x-ct)}{L} & , \quad ct-L < x < ct \\ 0 & , \quad x > ct \\ (t > 0) \end{cases}$$

where L is the wavelength and c is the convection speed. Each event was assumed to have unit magnitude and no decay of any type was assumed in order to show clearly the spatial and temporal resolution effects.

Since the wave front for $\Delta P(x,t)$, designated $X_f(t)$, is located by:

$$X_f(t) = ct$$

a contribution to the pressure force on a transducer located on the interval, $x_1 < x < x_2$, will be made when

$$X_f(t) > x_1$$

and

$$X_f(t) - L < x_2.$$

where the origin of the coordinate is sitting on the wavefront and is moving with the event convection speed, c .

Assuming the spanwise (Z) dimension of the transducer is unity, the incremental force contribution due to this pressure event at some time, t_n , which satisfies the wave front criteria ($\frac{x_1}{c} < t_n < \frac{x_2+L}{c}$) is given by:

$$\begin{aligned} F(t_n) &\equiv \frac{L}{2\pi} \int_{\theta_1}^{\theta_2} [\sin \theta - 1/2 \sin 2\theta] d\theta \\ &= \frac{\cos 2\theta_2 - \cos 2\theta_1}{4} + \cos \theta_1 - \cos \theta_2 \equiv \frac{2\pi F_n}{L} \end{aligned}$$

where

$$\theta_1 = \begin{cases} \frac{2\pi x_1}{L} & \text{when } X_f - L < x_1 \\ \frac{2\pi (X_f - L)}{L} & \text{when } X_f - L > x_1 \end{cases}$$

and

$$\theta_2 = \begin{cases} \frac{2\pi X_f}{L}, & \text{when } X_f < x_2 \\ \frac{2\pi x_2}{L}, & \text{when } X_f > x_2. \end{cases}$$

Consequently, the average incremental pressure contribution, $\Delta \bar{P}_n$, can be written:

$$\Delta \bar{P}_n = \frac{F_n}{x_2 - x_1} = \frac{L}{2\pi(x_2 - x_1)} \left\{ 1/4 [\cos 2\theta_2 - \cos 2\theta_1] + \cos \theta_1 - \cos \theta_2 \right\}^*$$

The time step discussion will be deferred temporarily and attention will be restricted to some time, t_n , when the disturbance is over the transducer. For very early times, the wave front will be over the transducer, while the trailing edge of the wave has not yet crossed the boundary, x_1 . (See Fig. A1). Then,

$$\text{while,} \quad \theta_2 = \frac{2\pi ct_n}{L}$$

$$\theta_1 = \frac{2\pi x_1}{L},$$

so that

$$\Delta \bar{P}_n = \frac{L}{2\pi(x_2 - x_1)} \left\{ 1/4 \left[\cos \frac{4\pi ct_n}{L} - \cos \frac{4\pi x_1}{L} \right] + \cos \frac{2\pi x_1}{L} - \cos \frac{2\pi ct_n}{L} \right\}.$$

For very late times,

$$\theta_1 = \frac{2\pi(ct_n - L)}{L},$$

while,

$$\theta_2 = \frac{2\pi x_2}{L},$$

*Integration can be checked by taking the limit as $x_1 \rightarrow x_2$, which restricts time so that $\theta_2 \rightarrow \theta_1$.

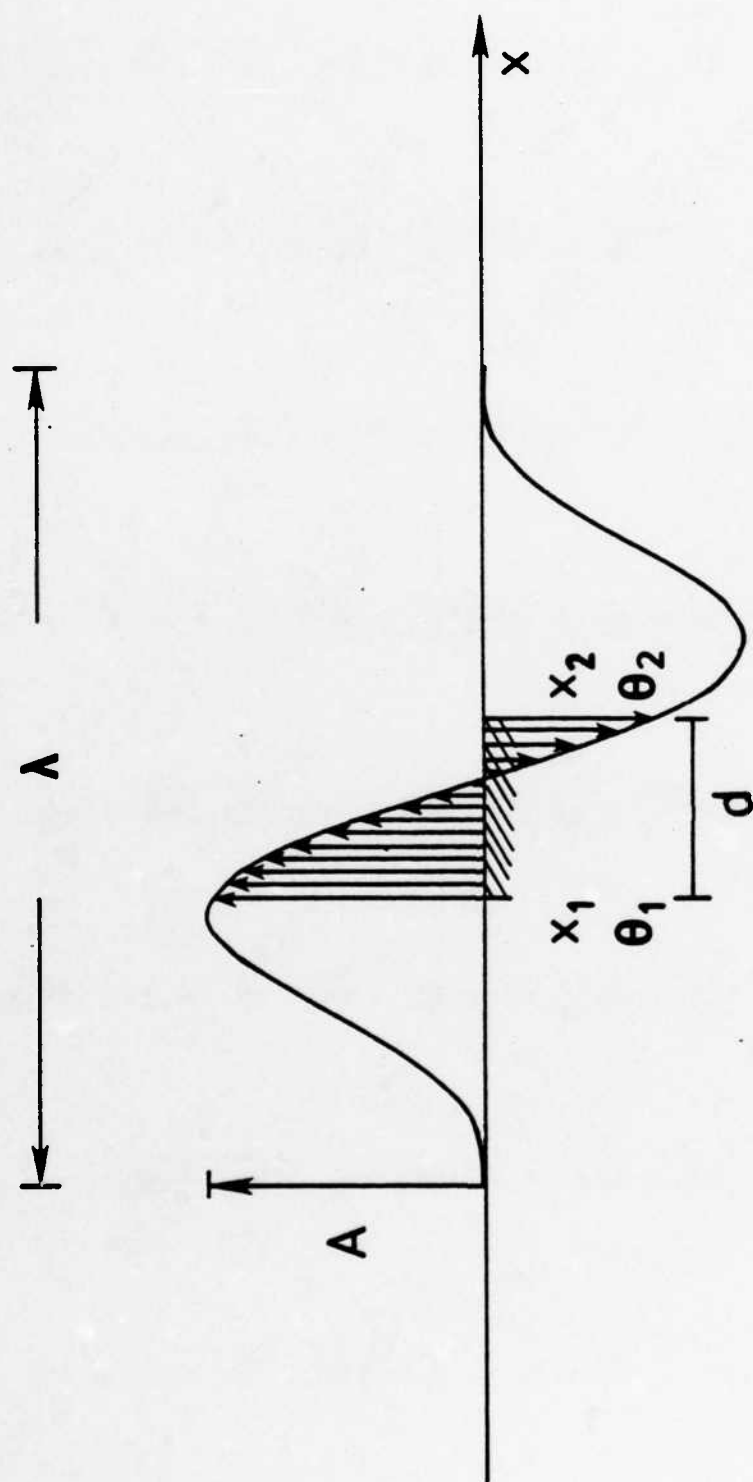


Figure A1. A picture of the prototype double sine wave moving over a transducer.

leaving

$$\Delta \bar{P}_n = \frac{L}{2\pi(x_2-x_1)} \left\{ 1/4 \left[\cos \frac{4\pi x_2}{L} - \cos \frac{2\pi ct_n}{L} \right] + \cos \frac{2\pi ct_n}{L} - \cos \frac{2\pi x_2}{L} \right\}.$$

Two types of wavelength cases are delineated by the case when $x_2-x_1 = L$. When the wavelength is greater than the transducer length, $L > x_2-x_1$, there will be times, t_n , when neither the wave front nor its trailing edge will be over the transducer, in which case

$$\Delta \bar{P}_n = \frac{L}{2\pi(x_2-x_1)} \left\{ 1/4 \left[\cos \frac{4\pi(ct_n-x_2)}{L} + \cos \frac{4\pi(x_1-L-ct_n)}{L} \right] + \cos \frac{2\pi(x_1-L-ct_n)}{L} - \cos \frac{2\pi(ct_n-x_2)}{L} \right\}.$$

When the wavelength is less than the transducer length, $L < x_2-x_1$, for,

$$\frac{x_1+L}{c} < t_n < \frac{x_2}{c},$$

$$\Delta \bar{P}_n = 0.$$

The second case in which $L < x_2-x_1$, is discussed next.

Figure A2 represents the averaged force as a function of time for a large transducer ($L < x_2-x_1$). That figure shows how the shape of the double sine wave is reinterpreted such that the negative and the positive pressure regions are separated by a dead band. This dead band is created during the time interval when the entire wave is over the trans-

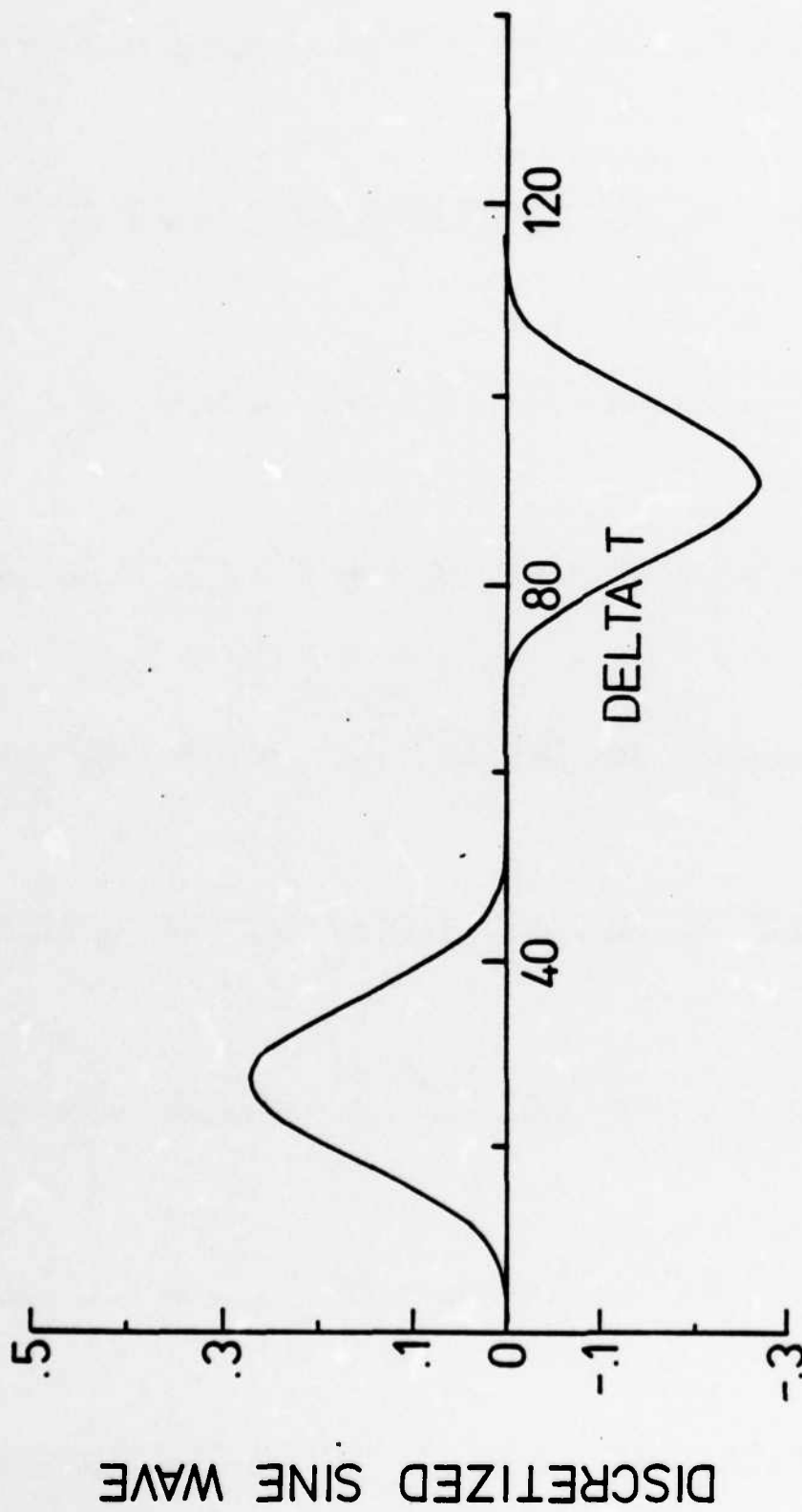


Figure A2. Averaged force as a function of time with a time step smaller than the simulation time step (Δt).

ducer. The same effect is also responsible for a significant change in the wavelength of the averaged transient force. The indicated wavelength will be twice that of the event when the transducer length, $x_2 - x_1$, is equal to L . When $x_2 - x_1$ is greater than L , the apparent wavelength is increased by more than a factor of two, as shown in the figure. Also note that the averaging caused by the transducer has a severe effect on the amplitude of the wave.

At this point, it should be pointed out that, in order to show the above effects as clearly as possible, the smooth curve of Fig. A2 has been obtained by employing a resolving time step which was an order of magnitude smaller than the time step used in the simulation. Therefore, the same case was repeated employing the nominal simulation time increment used in this study. The resulting curve is shown in Fig. A3. Although it is not a smooth curve anymore, the major features described above still are detectable.

A series of tests have been run for the case in which $L > x_2 - x_1$. In those tests the width of the sensing area has been kept constant at a value of $\frac{d}{\delta} = 0.176$, while the frequency of the wave and the resolving time step have been varied. Figure A4 shows a typical wave with a frequency of 300 Hz ($S_t = 0.287$) resolved by a time step which is an order of magnitude larger than the time step used in the simulation. The solid lines are the numerically integrated values, while the squares represent the theoretical wave at a point location. Although, the agreement between the two types of calculations is good, the figure does not carry sufficient information to represent the prototype double sine wave. Figure A5 shows the same wave resolved by a time step equal to

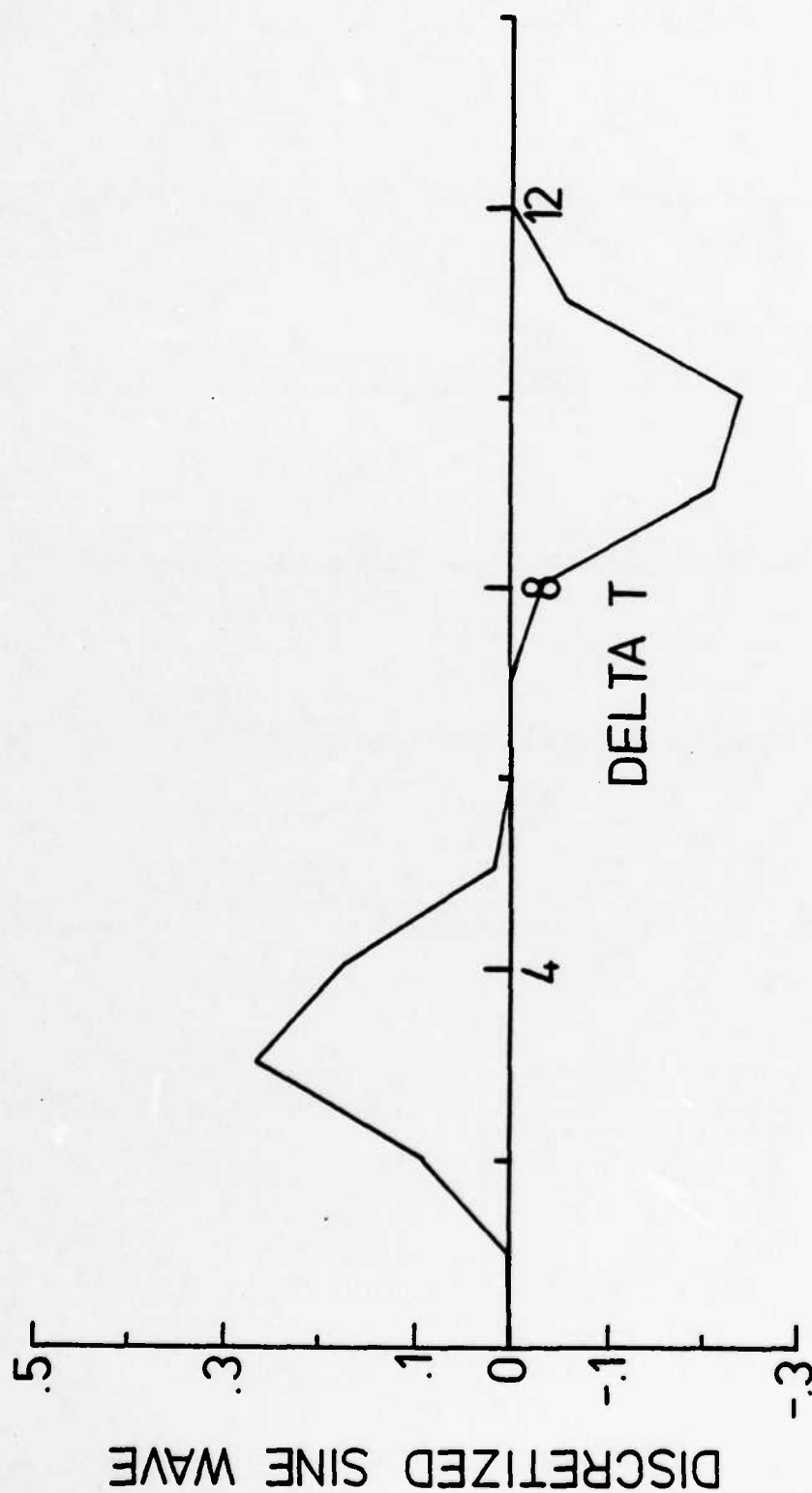


Figure A3. Averaged force as a function of time with a time step equal to the simulation time step (Δt).

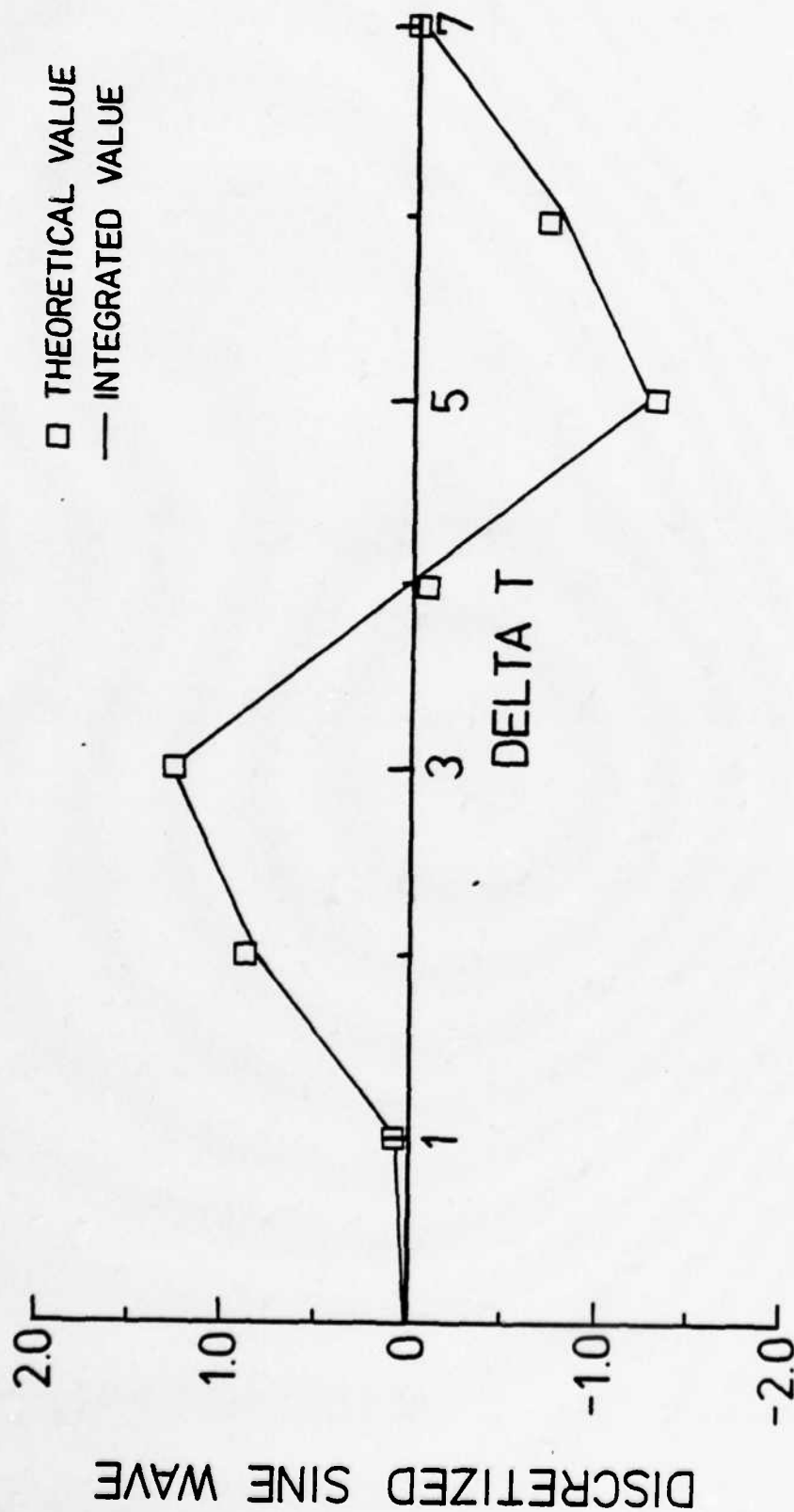


Figure A4. Temporal resolution of a large wavelength double sine wave with a time step greater than the simulation time step (Δt).

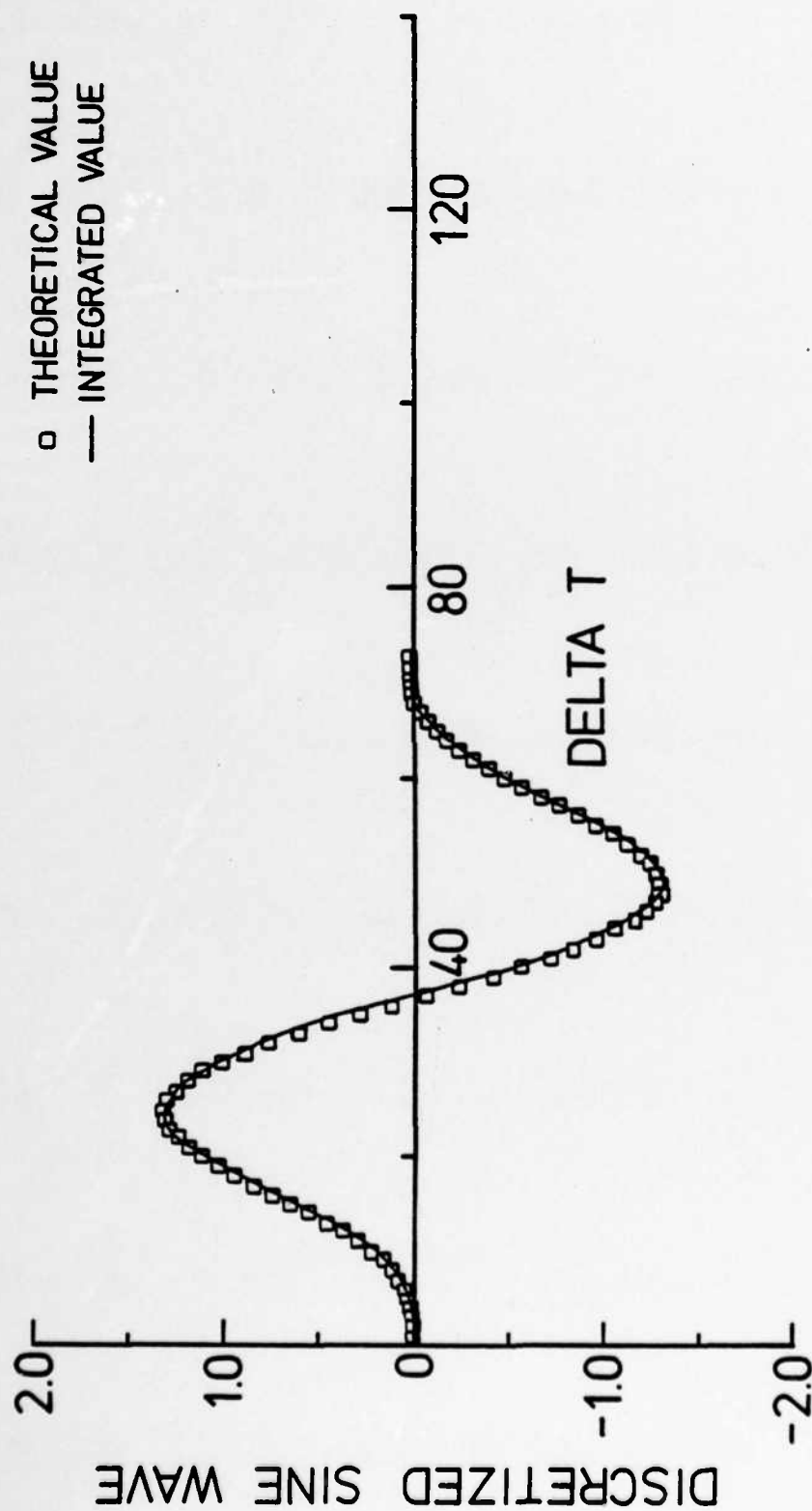


Figure A5. Temporal resolution of a large wavelength double sine wave with a time step equal to the simulation time step (Δt).

the simulation time step. The agreement between the two methods is excellent and the shape of a double sine wave is retained. Subsequently, the frequency of the wave was increased to 2500 Hz ($S_t=2.39$) while the resolving time step was kept constant. Figure A6 suggests that as the frequency of the wave is increased, the temporal resolution becomes a problem. Also, note that there is a phase shift between the two types of calculations. Figure A7 represents a wave with a frequency of 2500 Hz resolved by a time step which is an order of magnitude smaller than the time step used in the simulation. The above figure indicates that the resolution problem disappears as the time step approaches zero.

In summary, significant alterations of prototype high frequency pressure fluctuation events can occur due to transducer size and resolving time increment. But, as the wavelength of the individual event increases, the effects of transducer size and temporal resolution diminishes.

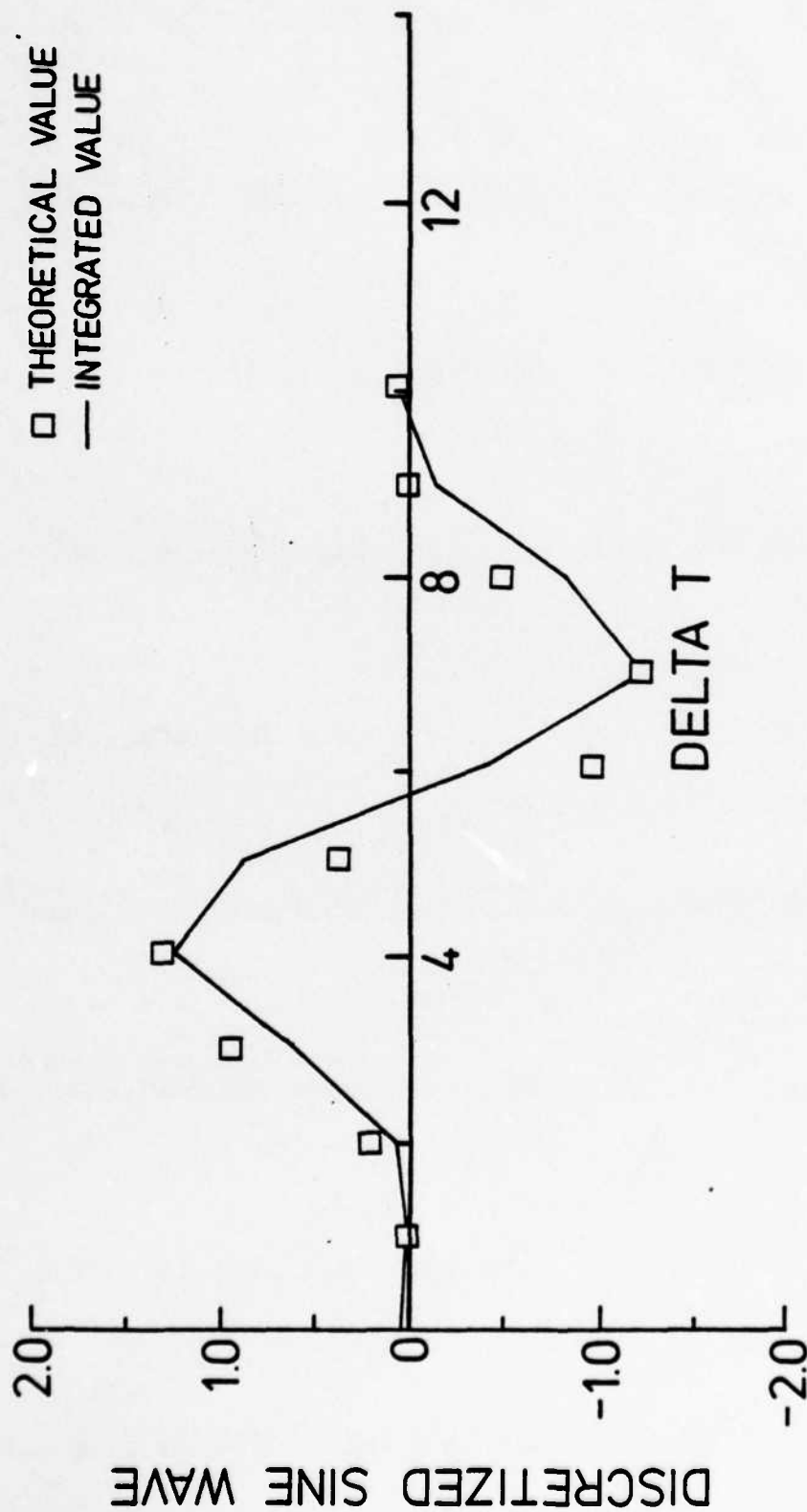


Figure A6. Temporal resolution of a small wavelength double sine wave with a time step equal to the simulation time step (Δt).

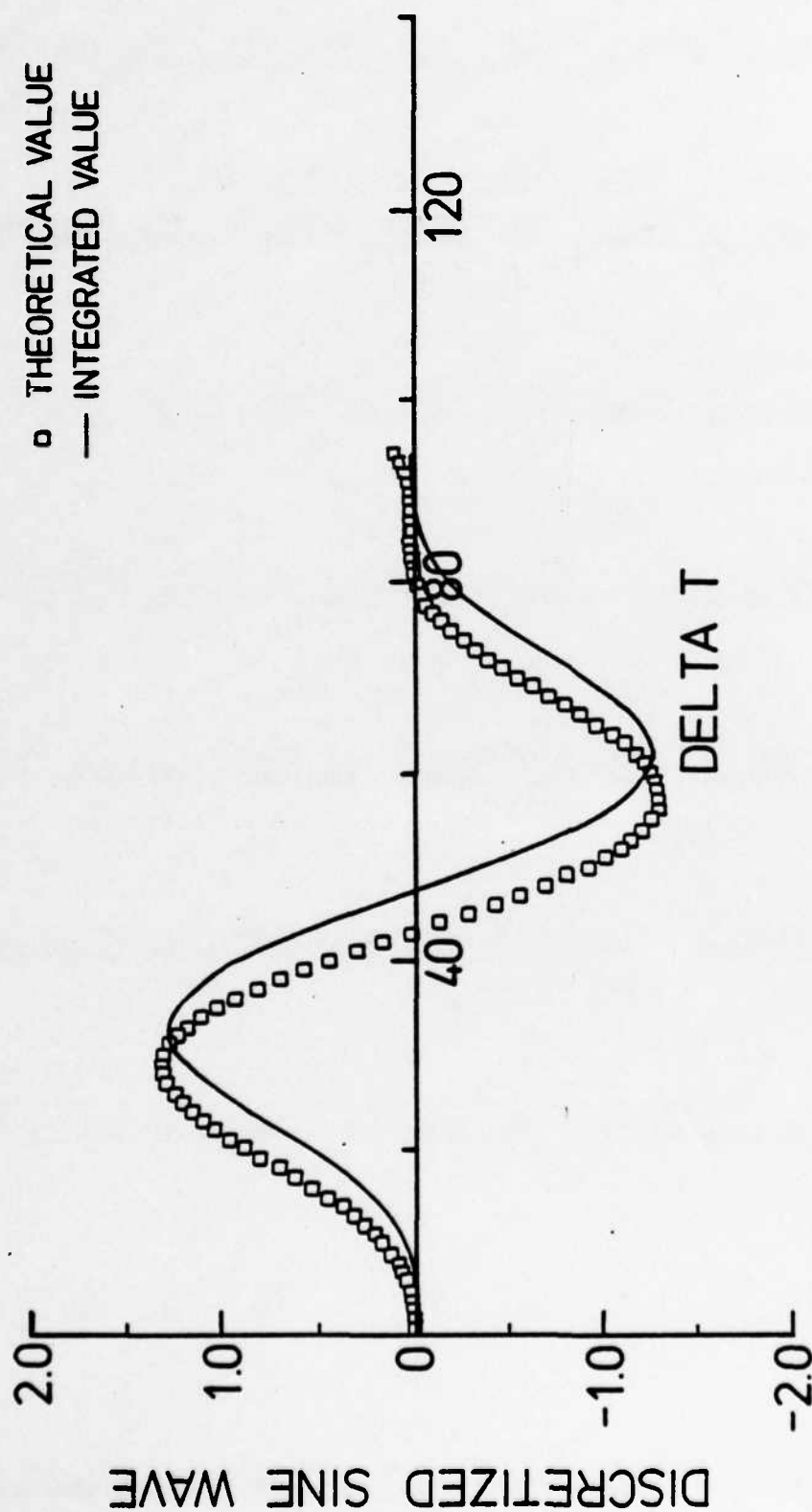


Figure A7. Temporal resolution of a small wavelength double sine wave with a time step smaller than the simulation time step (Δt).

APPENDIX B

COMPUTER PROGRAM LISTING

```

PROGRAM SIMU(INPUT,OUTPUT,TAPF5=INPUT,TAPE6=OUTPUT,TAPE1,TAPE2
1,TAPE7,TAPE8)
  DIMENSION P(5,16500)
  DIMENSION SUMX(8000),SUMY(8000)
  EQUIVALENCE(P(60000),SUMX),(P(74000),SUMY)
  DIMENSION PA(6),PR(6),STRT(6),STP(6)
  NR=5
  NW=6
C   NDIM=MAXIMUM TIME DIMENSION
  NDIM=16500
  N2C=NDIM/500
  CDIM=NDIM
C   CORX IS THE ADJUSTMENT FOR DX STREAK.
C   IF MORE THAN ONE BURST PER STREAK, CORX IS NOT UNITY
  CORX=1.5
C   CORT IS THE TIME ADJUSTMENT FOR DT-STREAK
  CORT=2.
C   XD=DEVELOPMENT LENGTH (M)
C   XM=MODEL LENGTH (M)
C   PAR IS THE DECAY ADJUSTMENT ACCOUNTING FOR DISTURBANCE SIZE
  PAR=10.
  XD=4.145
C   DXT IS THE DISTANCE BETWEEN STORAGE LOCATIONS
  DXT=0.008
  DWT=DXT
C   DWT IS THE WIDTH OF THE PRESSURE STORAGE LOCATION
  DWT=0.002
  IMJ=0
  XM=0.0
157 XD=XD+XM
  XT=XD+XM
C   DXT=NODE SPACING ON MODEL(M)
C   NXM IS THE NUMBER OF STORAGE LOCATIONS...YOU MUST CHANGE THE
C   NUMBERS IN THE DIMENSION STATEMENTS AND IN THE TAPE OUTPUT
  NXM=3
  STRT(1)=XD
  STP(1)=STRT(1)+DWT
  STRT(2)=XD+0.008466
  STP(2)=STRT(2)+DWT
  STRT(3)=XD+0.068187
  STP(3)=STRT(3)+DWT
  XSMX=2.0+STP(NXM)
C   XSMX IS THE RIGHT-MOST LOCATION STORING PRESSURE
  US=33.5
  BLT=0.0408
  UFRIC=1.2587
  CNU=0.00001395
  RHO=1.2
  DPT=BLT/8

```

```

C      ENTER OTHER DISPLACEMENT THICKNESS HERE IF DESIRED (CM)
C      DIMENSIONLESS STORAGE LOC. WIDTH--W/DISP. THICK.
      WDM=DWT/DPT
      WRITE(NW,205) WDM
205  FORMAT(///,5X,*DIM. STORAGE WIDTH EQ. *,E16.8,/)
      WRITE(NW,206)
206  FORMAT(5X,*LOCATION NO.          DIM. LOC.*,/)
      DO 30 I=1,NXM
      XDM=STRT(I)/DPT
      WRITE(NW,210) I,XDM
210  FORMAT(10X,I4,10X,E16.8)
      30 CONTINUE
C      CALCULATION OF WALL SHEAR STRESS, TW
      TW=RHO*UFRIC*UFRIC
C      CALCULATION OF RMS PRESSURE FLUCTUATION
      PRMS=2.0*TW
C      CALCULATION OF MINIMUM RELEVANT DISTURBANCE LENGTH
C      TWV IS TIME DURATION OF DISTURBANCE
      TWV=DPT/US
C      LENGTH OF SMALL DISTURBANCE
      CLM=0.7*US*TWV
C      DECAY RIAS PARAMETER
      CWV=PAR*CLM
      CWV=0.007
C      MISCELLANEOUS CONSTANTS
      PI=3.1415926
      TPI=2.*PI
      HPI=PI/2.
      C0=2.515517
      C1=0.802853
      C2=0.010328
      D1=1.432788
      D2=0.189269
      D3=0.001308
C      STARTER FOR RANDOM NUMBER GENERATOR
      XSTART=77294.
      RNM=URAN(XSTART)
      XSTART=0.0
C      CALCULATION OF NOMINAL PEAK FREQUENCY
      FPEAK=0.20574*US/(TPI*DPT)
      FMAX=10.*FPEAK
C      COMPATABLE TIME STEP
      DTT=1./FMAX/10.
C      A USER SPECIFIED TIME STEP CAN BE ENTERED HERE
C      THIS TIME STEP IS THE TIME INCREMENT USED IN THE RESOLUTION OF THE
C      OUTPUT--THE INTERNAL FLUCTUATION TIME STEP IS RANDOM
C      MAXIMUM TIME IS CONSTRAINED BY COMPUTER STORAGE. SET THE NUMBER
C      OF ALLOWABLE TIMESTEPS--NTM

```

```

      NTM=16500
C     INITIAL TIME IS TO(SEC)
      TO=0.
      DTSUM=0.
      NCT=1
C     PREFIXES FOR RANDOM NUMBER CALCULATIONS
      PX=DPT*UFRIC/US
      PT=DPT/US
      PW=US/DPT
C     CALCULATION OF REQUIRED START UP TIME FOR SIMULATION
      TSO=1.8*XT/US
      NMIN=TSO/DTT
      TMAX1=NMIN*DTT
C     IF NMIN IS GREATER THAN NTM, NTM IS OVERRIDDEN
      IF(NMIN-NTM)201,201,202
202   NTM=NMIN
201   CONTINUE
      TMAX=NTM*DTT
      WRITE(6,100) DTT,TMAX
100   FORMAT(5X,*DT=*,F10.8,10X,*TMAX=*,F10.4,/)
      TMAXS=CDIM*DTT
      TMAX=TMAX+TMAX1
      NTM2=NDIM-NMIN+2
      TREF=TMAX1
      NREL=0
C     INITIALIZE PRESSURE ARRAY
      DO 52 NX=1,NXM
      DO 52 NT=1,NDIM
52    P(NX,NT)=0.0
      NFLG=0
      TSUB=0.
C     INITIALIZE LOCATION AND TIME BASE, ETC.
      1 X=0.
      DTAVG=DTSUM/NCT
      NCT=0
      DTSUM=0.
      TO=TO+DTAVG
      IF(TO-TMAX1)2,150,150
150   IF(NFLG) 151,151,15
151   NFLG=1
      TMAX1=TMAX
      DO 153 J=NTM2,NDIM
      P(I,J)=0.0
153   CONTINUE
      TO=0.
154   CONTINUE
      TSUB=TREF
      TMAXS=TMAXS+TREF
      NREL=NMIN

```

```

2 RNM=URAN(XSTART)
RNM=0.005+0.99*RNM
C CALCULATION OF DX USING RANDOM NUMBER RNM
HPII=HPI*RNM
DX=PX*(32.2-2/(RNM+0.0619)+72.*RNM**2+0.63*TAN(HPII))
DX=CDRX*DX
X=X+DX
RNM=URAN(XSTART)
RNM=0.04+0.955*RNM
C CALCULATION OF RADIAN FREQ. FROM NEW RNM
SRNM=RNM**0.6667
RRNM=(1.-RNM)**0.74
FRNM=1/RRNM-1
W=PW*(0.523*FRNM+0.799*SRNM-0.785*RNM)
F=W/TPI
IF(F.GT.7300.)GO TO 85
DC=0.78-F/(105.*FPEAK)
UC=DC*US
GO TO 87
85 UC=0.46*US
87 TP=1/F
BOBFAC=4.605/((DPT/UC)**2)
DXE=UC*TP
XD=X-DXE
C XD IS THE ORIGIN OF THE SINE WAVE FLUCTUATION
C X IS THE FRONT OF THE SINE WAVE
C XS IS THE FIRST STATION AT WHICH P IS RECORDED.
C XS AND NXI WILL BE TAKEN AS THE FIRST STATION VALUES--THEN OVERIDDE
XS=XD
NXI=1
C CHECK TO SEE IF THE DISTURBANCE IS OVER THE MODEL
IF(XD-X)3,3,5
C IF THE DISTURBANCE IS OVER THE MODEL, HAS IT PASSED THE LAST DATA
C STATION
3 CONTINUE
IF(XD-XS*X)971,1,1
971 CONTINUE
IF(XD.LT.0.)GO TO 964
DO 43 I=1,NXM
NNP=XD/STP(I)
IF(NNP)961,962,963
961 NXI=1
GO TO 964
962 NXI=I
GO TO 964
963 CONTINUE
43 CONTINUE
964 CONTINUE
C NXI IS THE NUMBER OF THE FIRST STORAGE LOCATION

```

```

CXNI=NXI
5 CONTINUE
C GENERATION OF RANDOM TIME STEP
6 RNM=URAN(XSTART)
RNM=0.005+0.99*RNM
HPII=HPI*RNM
DT=PT*(32.2-2./(RNM+0.0619)+72.*RNM**2+0.63*TAN(HPII)).
DT=CORT*DT
T=T0+DT
NCT=NCT+1
DTSUM=DTSUM+DT
IF(X0.GT.STP(NXM))GO TO 2
C GENERATION OF GAUSSIAN RANDOM PRESSURE AMPLITUDE
RNM=URAN(XSTART)
CIND=RNM+0.5
IND=CIND
CIND=IND
PPP=2.*(1.-CIND)-1.
ARGR=RNM/(1.+CIND)
ARG=1./(ARGR*ARGR)
CT=ALOG(ARG)
CM=SQRT(CT)
PMG=CM-(CO+CM*(C1+CM*C2))/(1+CM*(D1+CM*(D2+CM*D3)))
XS=XS-DXT
PPP=5.9000*PPP
PE=PRMS*PMG*PPP
PE=2.0*PE
C MODIFICATION OF PRESSURE AMPLITUDE TO ADJUST RMS PRESSURE LEVEL
C DO LOOP FOR STEPPING THROUGH MODEL STORAGE LOCATIONS
DXE=DXE
DO 14 NX=NXI,NXM
DXE=DXE
C MODEL STATION X-LOCATION
XS=STRT(NX)
C ARRIVAL TIME OF PRESSURE FLUCTUATION
DXS=XS-X
ADX=ABS(DXS)
DXS=(DXS+ADX)/2.
TGO=DXS/UC+T
C FLUCTUATION DEPARTURE TIME
DXO=STP(NX)-XO
TSTP=DXO/UC+T
C DOES TSTP EXCEED TMAX
IF(TSTP-TMAXS)9,9,7
7 IF(TGO-TMAXS)8,8,13
8 NSTOP=NDIM
GO TO 10
9 NSTOP=TSTP/DTT
10 NGO=TGO/DTT

```

```

      IF(NGD-NREL)99,99,98
98  CONTINUE
      AGX=DXD**0.6
      ARG=-4.20*AGX
      DH=0.35+0.65*EXP(ARG)
      DXEE=DH*DXE
      DR=DXE-DXEE
      RE=DR/(DTT*UC)
      RE=RE+0.5
      NP=RE
      NSTOP=NSTOP-NP
      DXE=DXEE
      IF(DXE.LE.0.0001)GO TO 2
C    DO LOOP FOR SUCCESSIVE TIME CONTRIBUTIONS TO THE SAME X LOCATION
      DO 12 NT=NGD,NSTOP
      TC=NT*DTT
      DELT=TC-T
      XTF=X+UC*(DELT)
      XTB=XTF-DXE
      THET1=(XTF-STP(NX))*TPI/DXE
      TH1A=ABS(THET1)
      THET1=(THET1+TH1A)/2.
      THET2=(STRT(NX)-XTB)/DXE
      TH2A=ABS(THET2)
      THET2=TPI-(THET2+TH2A)*PI
      XOT=UC*DELT
      IF(XOT-0.0000001)19,19,18
18  CONTINUE
C    FREQUENCY DEPENDENT VARIABLE DECAY RATE ADJUSTMENT
      AR=XOT/DXXE
      ARGX=-2.84*(AR**0.30)
      IF(ARGX.LE.-30.)GO TO 73
      DECA=EXP(ARGX)
      GO TO 23
73  DECA=0.0
      GO TO 23
19  CONTINUE
      DECA=1.
23  CONTINUE
      DTH1=2.*THET1
      DTH2=2.*THET2
      CF1=(COS(DTH2)-COS(DTH1))/4.
      CF2=COS(THET1)-COS(THET2)
      DP=PE*(CF1+CF2)
      DP=DP*DECA*DXE/(TPI*DWT)
      BOBBA=BOBFAC*DELT**2$IF(BOBBA.GT.300.)BOBBA=300.0
      DP=DP*(1.-EXP(-BOBBA))
      NTIME=NT-NREL
      P(NX,NTIME)=P(NX,NTIME)+DP

```



```

12 CONTINUE
99 CONTINUE
13 CONTINUE
14 CONTINUE
130 FORMAT(5X,F10.6,6E14.6)
GO TO 2
15 CONTINUE
NWRT=NTM/8
CNT=NTM
DO 11 J=1,NXM
PA(J)=0.0
11 PR(J)=0.0
DO 21 J=1,NXM
DO 20 I=1,NTM
PFI=P(J,I)
PA(J)=PA(J)+PFI
PR(J)=PR(J)+PFI*PFI
20 CONTINUE
PA(J)=PA(J)/CNT
WRITE(NW,192)J,PA(J)
PSJ=PA(J)*PA(J)
PRJ=PR(J)/CNT
PR(J)=SQRT(PRJ-PSJ)
PRMSR=PR(J)/PRMS
WRITE(NW,193)J,PR(J),PRMSR
21 CONTINUE
DO 22 J=1,NXM
DO 22 I=1,NTM
22 P(J,I)=P(J,I)-PA(J)
NYM=8000
ANN=NYM
NKL=NXM-1
DO 24 KK=1,NKL
DO 25 K=1,500
K1=K-1
SUM=0.
SM=0.$SKKM=0.$SKKOMK=0.$SKKMK=0.
SUM1=0.
DO 40 M=1,NYM
SUM=SUM+P(KK,M)*P(KK,M+K1)
SUM1=SUM1+P(1,M)*P(KK+1,M+K1)
SKKM=SKKM+P(KK,M)**2
SKKMK=SKKMK+P(KK,M+K1)**2
SM=SM+P(1,M)**2
SKKOMK=SKKOMK+P(KK+1,M+K1)**2
40 CONTINUE
SKKM=SQRT(SKKM/ANN)
SKKMK=SQRT(SKKMK/ANN)
SM=SQRT(SM/ANN)

```

```

      SKKOMK=SORT(SKKOMK/ANN)
      SUMX(K)=SUM/ANN/SKKM/SKKMK
      SUMY(K)=SUM1/ANN/SKKOMK/SM
25  CONTINUE
      WRITE(NW,191)
      WRITE(NW,200)(SUMX(K),K=1,500)
      WRITE(NW,191)
      WRITE(NW,200)(SUMY(K),K=1,500)
24  CONTINUE
191  FORMAT(1H1)
192  FORMAT(/,5X,"UNCORRECTED PAVG(",I3," ) IS",E20.6)
193  FORMAT(10X,"CORRECTED PRMS(",I3," ) IS",E20.6," RATIO",F10.3)
200  FORMAT(5E20.6)
      JXY=5500
      DO 93 J=1,NXM
      WRITE(1)(P(J,KJ),KJ=1,16500)
93  CONTINUE
1000 STOP
      END

```

DISTRIBUTION LIST FOR UNCLASSIFIED
TECHNICAL REPORTS AND REPRINTS ISSUED UNDER
CONTRACT N00014-82-K-0639 TASK NR 657-694

All addressees receive one copy unless otherwise specified.

Defense Technical Information Center
Cameron Station
Alexandria, VA 22314 12 copies

Professor Bruce Johnson
U.S. Naval Academy
Engineering Department
Annapolis, MD 21402

Library
U.S. Naval Academy
Annapolis, MD 21402

Technical Library
David W. Taylor Naval Ship Research
and Development Center
Annapolis Laboratory
Annapolis, MD 21402

Professor C. -S. Yih
The University of Michigan
Department of Engineering Mechanics
Ann Arbor, MI 48109

Professor T. Francis Ogilvie
The University of Michigan
Department of Naval Architecture
and Marine Engineering
Ann Arbor, MI 48109

Office of Naval Research
Code 200B
800 N. Quincy Street
Arlington, VA 22217

Office of Naval Research
Code 438
800 N. Quincy Street
Arlington, VA 22217 3 copies

Office of Naval Research
Code 473
800 N. Quincy Street
Arlington, VA 22217

NASA Scientific and Technical
Information Facility
P. O. Box 8757
Baltimore/Washington International
Airport
Maryland 21240

Professor Paul M. Naghdi
University of California
Department of Mechanical Engineering
Berkeley, CA 94720

Librarian
University of California
Department of Naval Architecture
Berkeley, CA 94720

Professor John V. Wehausen
University of California
Department of Naval Architecture
Berkeley, CA 94720

Library
David W. Taylor Naval Ship Research
and Development Center
Code 522.1
Bethesda, MD 20084

Mr. Justin H. McCarthy, Jr.
David W. Taylor Naval Ship Research
and Development Center
Code 1552
Bethesda, MD 20084

Dr. William B. Morgan
David W. Taylor Naval Ship Research
and Development Center
Code 1540
Bethesda, MD 20084

Director
Office of Naval Research Eastern/Central
Building 114, Section D Regional Office
666 Summer Street
Boston, MA 02210

Library
Naval Weapons Center
China Lake, CA 93555

Technical Library
Naval Surface Weapons Center
Dahlgren Laboratory
Dahlgren, VA 22418

Technical Documents Center
Army Mobility Equipment Research Center
Building 315
Fort Belvoir, VA 22060

Technical Library
Webb Institute of Naval Architecture
Glen Cove, NY 11542

Dr. J. P. Breslin
Stevens Institute of Technology
Davidson Laboratory
Castle Point Station
Hoboken, NJ 07030

Professor Louis Landweber
The University of Iowa
Institute of Hydraulic Research
Iowa City, IA 52242

R. E. Gibson Library
The Johns Hopkins University
Applied Physics Laboratory
Johns Hopkins Road
Laurel, MD 20810

Lorenz G. Straub Library
University of Minnesota
St. Anthony Falls Hydraulic Laboratory
Minneapolis, MN 55414

Library
Naval Postgraduate School
Monterey, CA 93940

Technical Library
Naval Underwater Systems Center
Newport, RI 02840

Engineering Societies Library
345 East 47th Street
New York, NY 10017

The Society of Naval Architects and
Marine Engineers
One World Trade Center, Suite 1369
New York, NY 10048

Technical Library
Naval Coastal System Laboratory
Panama City, FL 32401

Professor Theodore Y. Wu
California Institute of Technology
Engineering Science Department
Pasadena, CA 91125

Director
Office of Naval Research Western Region
1030 E. Green Street Office
Pasadena, CA 91101

Technical Library
Naval Ship Engineering Center
Philadelphia Division
Philadelphia, PA 19112

Army Research Office
P. O. Box 12211
Research Triangle Park, NC 27709

Editor
Applied Mechanics Review
Southwest Research Institute
8500 Culebra Road
San Antonio, TX 78206

Technical Library
Naval Ocean Systems Center
San Diego, CA 92152

ONR Scientific Liaison Group
American Embassy - Room A-407
APO San Francisco 96503

Librarian
Naval Surface Weapons Center
White Oak Laboratory
Silver Spring, MD 20910

Defense Research and Development Attache
Australian Embassy
1601 Massachusetts Avenue, NW
Washington, DC 20036

Librarian Station 5-2
Coast Guard Headquarters
NASSIF Building
400 Seventh Street, SW
Washington, DC 20591

Library of Congress
Science and Technology Division
Washington, DC 20540

Dr. A. L. Slafkowsky
Scientific Advisor
Commandant of the Marine Corps
Code AX
Washington, DC 20380

Maritime Administration
Office of Maritime Technology
14th & E Streets, NW
Washington, DC 20230

Maritime Administration
Division of Naval Architecture
14th & E Streets, NW
Washington, DC 20230

Dr. G. Kulin
National Bureau of Standards
Mechanics Section
Washington, DC 20234

Naval Research Laboratory
Code 2627
Washington, DC 20375 6 copies

Library
Naval Sea Systems Command
Code 09GS
Washington, DC 20362

Mr. Thomas E. Peirce
Naval Sea Systems Command
Code 03512
Washington, DC 20362

Mr. Stanley W. Doroff
Mechanical Technology, Inc.
2731 Prosperity Avenue
Fairfax, VA 22031

Dr. Charles Watkins
Head, Mechanical Engineering Department
Howard University
Washington, DC 20059

DISTRIBUTION LIST FOR UNCLASSIFIED
TECHNICAL REPORTS AND REPRINTS ISSUED UNDER
CONTRACT N00014-82-K-0639 TASK NR 657-694

Professor W. W. Willmarth
The University of Michigan
Department of Aerospace Engineering
Ann Arbor, MI 48109

Office of Naval Research
Code 481
800 N. Quincy Street
Arlington, VA 22217

Professor Richard W. Miksad
The University of Texas at Austin
Department of Civil Engineering
Austin, TX 78712

Professor Stanley Corrsin
The Johns Hopkins University
Department of Mechanics and
Materials Sciences
Baltimore, MD 21218

Professor Paul Lieber
University of California
Department of Mechanical Engineering
Berkeley, CA 94720

Professor P. S. Virk
Massachusetts Institute of Technology
Department of Chemical Engineering
Cambridge, MA 02139

Professor E. Mollo-Christensen
Massachusetts Institute of Technology
Department of Meteorology
Room 54-1722
Cambridge, MA 02139

Professor Patrick Leehey
Massachusetts Institute of Technology
Department of Ocean Engineering
Cambridge, MA 02139

Professor Eli Reshotko
Case Western Reserve University
Department of Mechanical and
Aerospace Engineering
Cleveland, OH 44106

Professor S. I. Pai
University of Maryland
Institute of Fluid Dynamics
and Applied Mathematics
College Park, MD 20742

Computation and Analyses Laboratory
Naval Surface Weapons Center
Dahlgren Laboratory
Dahlgren, VA 22418

Dr. Robert H. Kraichnan
Dublin, NH 03444

Professor Robert E. Falco
Michigan State University
Department of Mechanical Engineering
East Lansing, MI 48824

Professor E. Rune Lindgren
University of Florida
Department of Engineering Sciences
231 Aerospace Engineering Building
Gainesville, FL 32611

Mr. Dennis Bushnell
NASA Langley Research Center
Langley Station
Hampton, VA 23365

Dr. A. K. M. Fazle Hussain
University of Houston
Department of Mechanical Engineering
Houston, TX 77004

Professor John L. Lumley
Cornell University
Sibley School of Mechanical
and Aerospace Engineering
Ithaca, NY 14853

Professor K. E. Shuler
University of California, San Diego
Department of Chemistry
La Jolla, CA 92093

Dr. E. W. Montroll
Physical Dynamics, Inc.
P. O. Box 556
La Jolla, CA 92038

Dr. Steven A. Orszag
Cambridge Hydrodynamics, Inc.
54 Baskin Road
Lexington, MA 02173

Professor Tuncer Cebeci
California State University
Mechanical Engineering Department
Long Beach, CA 90840

Dr. C. W. Hirt
University of California
Los Alamos Scientific Laboratory
P. O. Box 1663
Los Alamos, NM 87544

Professor Frederick K. Browand
University of Southern California
University Park
Department of Aerospace Engineering
Los Angeles, CA 90007

Professor John Laufer
University of Southern California
University Park
Department of Aerospace Engineering
Los Angeles, CA 90007

Professor T. R. Thomas
Teesside Polytechnic
Department of Mechanical Engineering
Middlesbrough TS1 3BA, England

Dr. Arthur B. Metzner
University of Delaware
Department of Chemical Engineering
Newark, DE 19711

Professor Harry E. Rauch
The Graduate School and University
Center of the City University of
New York
Graduate Center: 33 West 42 Street
New York, NY 10036

Mr. Norman M. Nilsen
Dyntec Company
5301 Laurel Canyon Blvd., Suite 201
North Hollywood, CA 91607

Professor L. Gary Leal
California Institute of Technology
Division of Chemistry and Chemical
Engineering
Pasadena, CA 91125

Professor H. W. Liepmann
California Institute of Technology
Graduate Aeronautical Laboratories
Pasadena, CA 91125

Professor A. Roshko
California Institute of Technology
Graduate Aeronautical Laboratories
Pasadena, CA 91125

Dr. Leslie M. Mack
Jet Propulsion Laboratory
California Institute of Technology
Pasadena, CA 91103

Professor K. M. Agrawal
Virginia State College
Department of Mathematics
Petersburg, VA 23803

Technical Library
Naval Missile Center
Point Mugu, CA 93041

Professor Francis R. Hama
Princeton University
Department of Mechanical and
Aerospace Engineering
Princeton, NJ 08540

Dr. Joseph H. Clarke
Brown University
Division of Engineering
Providence, RI 02912

Professor J. T. C. Liu
Brown University
Division of Engineering
Providence, RI 02912

Chief, Document Section
Redstone Scientific Information Center
Army Missile Command
Redstone Arsenal, AL 35809

Dr. Jack W. Hoyt
Naval Ocean Systems Center
Code 2501
San Diego, CA 92152

Professor Richard L. Pfeffer
Florida State University
Geophysical Fluid Dynamics Institute
Tallahassee, FL 32306

Dr. Denny R. S. Ko
Dynamics Technology, Inc.
22939 Hawthorne Boulevard, Suite 200
Torrance, CA 90505

Dr. Gary Chapman
Ames Research Center
Mail Stop 227-4
Moffett Field, CA 94035

Professor Thomas J. Hanratty
University of Illinois at Urbana-
Champaign
Department of Chemical Engineering
205 Roger Adams Laboratory
Urbana, IL 61801

Air Force Office of Scientific
Research/NA
Building 410
Bolling AFB
Washington, DC 20332

Professor Hsien-Ping Pao
The Catholic University of America
Department of Civil Engineering
Washington, DC 20064

Dr. Phillip S. Klebanoff
National Bureau of Standards
Mechanics Section
Washington, DC 20234

Dr. G. Kulin
National Bureau of Standards
Mechanics Section
Washington, DC 20234

Dr. J. O. Elliot
Naval Research Laboratory
Code 8310
Washington, DC 20375

Mr. R. J. Hansen
Naval Research Laboratory
Code 8441
Washington, DC 20375

END

FILMED

9-83

DTIC